

**The effect of liquid co-flow on gas fractions, bubble velocities and chord lengths in bubbly flows. Part II**

**Asymmetric flow configurations**

Muilwijk, Corné; Van den Akker, Harry E.A.

**DOI**

[10.1016/j.ijmultiphaseflow.2021.103562](https://doi.org/10.1016/j.ijmultiphaseflow.2021.103562)

**Publication date**

2021

**Document Version**

Final published version

**Published in**

International Journal of Multiphase Flow

**Citation (APA)**

Muilwijk, C., & Van den Akker, H. E. A. (2021). The effect of liquid co-flow on gas fractions, bubble velocities and chord lengths in bubbly flows. Part II: Asymmetric flow configurations. *International Journal of Multiphase Flow*, 138, Article 103562. <https://doi.org/10.1016/j.ijmultiphaseflow.2021.103562>

**Important note**

To cite this publication, please use the final published version (if applicable). Please check the document version above.

**Copyright**

Other than for strictly personal use, it is not permitted to download, forward or distribute the text or part of it, without the consent of the author(s) and/or copyright holder(s), unless the work is under an open content license such as Creative Commons.

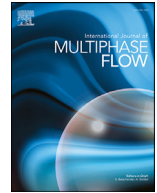
**Takedown policy**

Please contact us and provide details if you believe this document breaches copyrights. We will remove access to the work immediately and investigate your claim.



Contents lists available at ScienceDirect

## International Journal of Multiphase Flow

journal homepage: [www.elsevier.com/locate/ijmulflow](http://www.elsevier.com/locate/ijmulflow)

# The effect of liquid co-flow on gas fractions, bubble velocities and chord lengths in bubbly flows. Part II: Asymmetric flow configurations

Corné Muilwijk<sup>a,\*</sup>, Harry E.A. Van den Akker<sup>a,b</sup><sup>a</sup> Bernal Institute, University of Limerick, Limerick, V94 T9PX Ireland<sup>b</sup> Transport Phenomena Lab, Department of Chemical Engineering, Delft University of Technology, Van der Maasweg 9, 2629 HZ Delft, The Netherlands

## ARTICLE INFO

## Article history:

Received 8 April 2020

Revised 8 December 2020

Accepted 3 January 2021

Available online 10 January 2021

## Keywords:

Inhomogeneous Bubble column

Bubble Image Velocimetry

Optical fibre probe

CFD Validation

Gas hold-up

Mixing pattern

## ABSTRACT

This paper describes the effects of uniform and non-uniform liquid co-flow on the bubbly flow in a rectangular column (with two inlets) deliberately aerated unevenly. The two vertical bubbly streams, comprising uniform bubbles, started interacting downstream of the trailing edge of a splitter plate. This study quantifies the emergence of buoyancy driven flow patterns as a function of the degree of a-symmetric gas sparging and (non-)uniform liquid co-flow by using Bubble Image Velocimetry (BIV) and dual-tip optical fibre probes. Without liquid co-flow, small differences in the gas fraction of the left and right inlet had a large effect on the mixing pattern, whereas a liquid co-flow stabilized a homogeneous flow regime and the flow pattern was less sensitive to gas fraction differences. Void fractions, bubble velocities and chord lengths were measured at two fixed position in the flow channel, whereas BIV provided a global overview of the flow structures. A correlation was developed to predict (a-symmetric) operating conditions for which the gas fraction of the left and right inlet are balanced, such that the bubble motion is governed by advection and no buoyancy driven flow structures arise. The data obtained is highly valuable for CFD validation and development purposes.

© 2021 The Authors. Published by Elsevier Ltd.

This is an open access article under the CC BY license (<http://creativecommons.org/licenses/by/4.0/>)

## 1. Introduction

Besides classic symmetric bubble columns (with or without a liquid co/counter-current flow), a-symmetric bubble configurations are also widely encountered in the form of air-lift reactors and photobioreactors. It has been found that depending on the degree of a-symmetry and the emerging large scale motions, mixing times in laboratory scale setups are significantly reduced [Alm eras et al. (2018); McClure et al. (2016)] and heat transfer rates increased [Gvozdi c et al. (2019b)].

Scaling-up of bubble columns and aerated vessels requires detailed CFD modelling of the dispersed gas-liquid flow [Becker et al. (1994)]. Most of the available models work well for homogeneously dispersed bubbly flows and are used with increasing confidence, but modeling of a-symmetrically (or half) sparged bubble columns has proven to be a real challenge [Huang et al. (2018)]. Therefore, systematic and accurate experimental data, comprising gas fractions, bubble velocities and sizes and liquid velocities, in a-symmetric bubble column configurations

is crucial for CFD validation and development purposes, but it is sparsely available [De Tournemine and Roig (2010)].

Operating our rectangular bubble column a-symmetrically, i.e. by applying different air and/or water flow rates to the left-hand and right-hand sides, may create two parallel bubbly flows with different (mixture) velocities and/or (mixture) densities. The shear between these two parallel flows may result in Kelvin-Helmholtz (KH) instabilities which have been widely studied under single-phase conditions. Brown and Roshko (1974) experimented with parallel flows of two different gases and observed organized vortical flow structures which by pairing (see e.g., Winant and Browand (1974)) gave rise to a mixing layer between the two gas flows. The lateral growth of the mixing layer then follows from engulfment of outer fluid by these vortical structures. When conceiving bubbly flows as single-fluid flows comprising interpenetrating phases and exhibiting a mixture velocity, one could argue a similarity with the above single-phase KH instabilities. An analogy between single-phase and two-phase vortical structures has already been submitted a long time ago [Rietema (1982); Van Den Akker (1998)]. Groen et al. (1996) as well as Mudde and Van Den Akker (1999) observed and described dynamic behaviour of bubble columns comprising coherent vortical structures.

\* Corresponding author.

E-mail addresses: [Corne.Muilwijk@ul.ie](mailto:Corne.Muilwijk@ul.ie) (C. Muilwijk), [Harry.VanDenAkker@ul.ie](mailto:Harry.VanDenAkker@ul.ie) (H.E.A. Van den Akker).

Loth and Cebrzynski (1995) studied mixing layers between just a liquid and a liquid with bubbles 2 and 4 mm in diameter. They found these bubbles modulated shear layer thickness. Roig et al. (1998) reported results from just four experiments for a mixing layer between two bubbly flows with a low holdup (<2%) of bubbles with an average chord length of some 2 mm. They found the global behaviour of such bubbly flows to be very sensitive to (initial) void fraction contrasts. Ayed et al. (2007) injected millimetre sized oxygen bubbles by 576 small capillaries (0.33 mm internal diameter) at the low velocity side of a mixing layer, while no bubbles were introduced at the high velocity side. In a similar test facility, De Tournemine and Roig (2010) found stable flow patterns characterized by so-called frontiers between the bubbly streams from the left and right inlets. They only observed such frontiers when bubbles were injected on the low liquid velocity side, whereas oscillating boundaries occurred for all cases when bubbles were supplied at the high liquid velocity side.

These previous investigations of bubbly mixing layers [Roig et al. (1998); Ning et al. (2009); De Tournemine and Roig (2010)], seeded with (polydisperse) small bubbles and operated at low gas fractions, reported data for a very small number of cases only at seemingly arbitrary operating conditions. Therefore we identified an urgent need of a broader and more accurate database for a-symmetrically operated bubble columns: how asymmetric gas sparging induces dynamic buoyancy-driven flow behavior and how uniform and non-uniform liquid co-flow modifies this. A parametric study then delivers unique and highly valuable experimental data to serve as a reference for CFD validation in an Euler-Euler framework. While two parallel bubbly flows (separated by a boundary) develop in vertical direction, the strength of the buoyancy driven flow structures (e.g. liquid entrainment rates into a dense bubble swarm) as a function of the degree of a-symmetry can serve as a very strong benchmark case to calibrate sub-models for interfacial momentum transfer, two-phase turbulence and lateral dispersion of bubbles.

All these sub-models are strong functions of the (local) void fraction and bubble size (distribution). Therefore, computationally simulating half-sparged bubble columns as in Ayed et al. (2007); De Tournemine and Roig (2010); McClure et al. (2017, 2016) and Gvozdić et al. (2019a), axisymmetric non-uniform aeration in a cylindrical bubble column as in Hartevelde et al. (2003), or symmetric non-uniform sparging in a shallow 2D column as in Hartevelde (2005) is essentially easier when there is only a single bubble size (distribution) present. Of course, the bubble size depends on the gas flow rate and co-flow velocity Muilwijk and Van den Akker (2019a,b); Muilwijk and Van den Akker (2021). A-symmetric sparging in a bubble column then imposes different bubble sizes for each inlet, unless single bubbles are formed with a constant diameter at low, constant, gas flow rates in quiescent water as in Almérás et al. (2018), or in case a different splitter plate design is used as in Ning et al. (2009), where the independent control of both inlets was compromised. In our case, we designed the gas sparger in such a way, that (in each inlet) uniform large bubbles were produced, which essentially have constant rise velocities, such that lateral dispersion due to size/velocity differences, is minimized (as explained in Part I) and breakup and coalescence of bubbles is avoided.

Experiments were carried out in the test setup as described in our previous paper [Muilwijk and Van den Akker (2019b)], where the superficial liquid and gas velocities of both the left and right inlet compartments can be varied independently. The bubble size  $d_b$  in each inlet can be calculated using a correlation developed in our previous paper [Muilwijk and Van den Akker (2019b)] as a function of the sectional  $U_{sg}$  and  $U_{sl}$ .

For this Part II paper, we used the same techniques as described in Part I of this twin paper, viz. Bubble Image Velocimetry

(BIV) and dual-tip optical fibre probes (OFP), where BIV was used to perform analyses of the large scale flow structures, while the OFPs were used to measure local gas fractions, bubble velocities and chord lengths at fixed positions. Experiments were designed to cover a wide range of flow behaviors, such that a comprehensive set of experimental data was obtained.

A model to describe the gas fraction was adopted to predict a-symmetric operating conditions for which a higher gas flow rate is compensated with a higher liquid co-flow such that there is no gas fraction difference at sparger level. For these conditions, where no buoyancy driven flow structures emerge and the bubble motion was governed by advection, bubbly mixing layer patterns occur. We then also identified operating conditions for which there are, in addition to an equal gas fraction at left and right inlet, (almost) equal bubble sizes formed in both inlet sections.

The structure of this paper is then as follows. An overview of experimental parameters and the different flow configuration scenarios is given in Sec. 2; Sec. 3 shows results on the effect of a uniform liquid co-flow on the flow patterns and the departure from symmetric operation with increasing degrees of a-symmetric gas sparging. Sec. 4 presents results on the effect of uneven (left and right inlet) liquid co-flows on flow patterns. Concluding remarks and suggestions for future work are given in Sec. 5.

## 2. Methods and parameters

Measurements were carried out in the "LimBuRig" test facility [Muilwijk and Van den Akker (2019b)]. Two, initially separated, parallel streams of bubbly flows with different superficial (gas and liquid) velocities, started interacting downstream of the trailing edge of a splitter plate (see Fig. 1a). While Part I of this paper showed results for a symmetric operation (uniform  $U_{sg}$  and  $U_{sl}$ ), a-symmetric bubble column configurations were studied for this part, where the superficial gas velocities  $U_{sg}$  and/or superficial liquid velocities  $U_{sl}$  (Left and Right) were varied independently. In Fig. 1a, the gas flow is higher at the right hand side, while the liquid flow rate is highest in the left compartment. Downstream of the splitter plate, the fast liquid flow from the left inlet slows down and expands laterally, pushing the flow with the higher void fraction to the right; the latter then starts accelerating due to increased buoyancy. K-H instabilities develop the growth of which is restricted by the close proximity of the right side wall. The various flow cases are described with the help of the following parameters:

$$\langle U_{sg} \rangle = \frac{1}{2} (U_{sg,L} + U_{sg,R}) \quad (1)$$

$$\langle U_{sl} \rangle = \frac{1}{2} (U_{sl,L} + U_{sl,R}) \quad (2)$$

$$\Delta U_{sg} = U_{sg,R} - U_{sg,L} \quad (3)$$

$$\Delta U_{sl} = U_{sl,R} - U_{sl,L} \quad (4)$$

where  $L, R$  denote the left and right inlet, respectively. The degrees of a-symmetry in the superficial gas and liquid velocity,  $\lambda_g$  and  $\lambda_l$  respectively, were then defined as the ratio of the superficial gas or liquid velocity difference (between left and right inlet) to the mean superficial velocity:

$$\lambda_g = \frac{\Delta U_{sg}}{\langle U_{sg} \rangle} \quad (5)$$

$$\lambda_l = \frac{\Delta U_{sl}}{\langle U_{sl} \rangle} \quad (6)$$

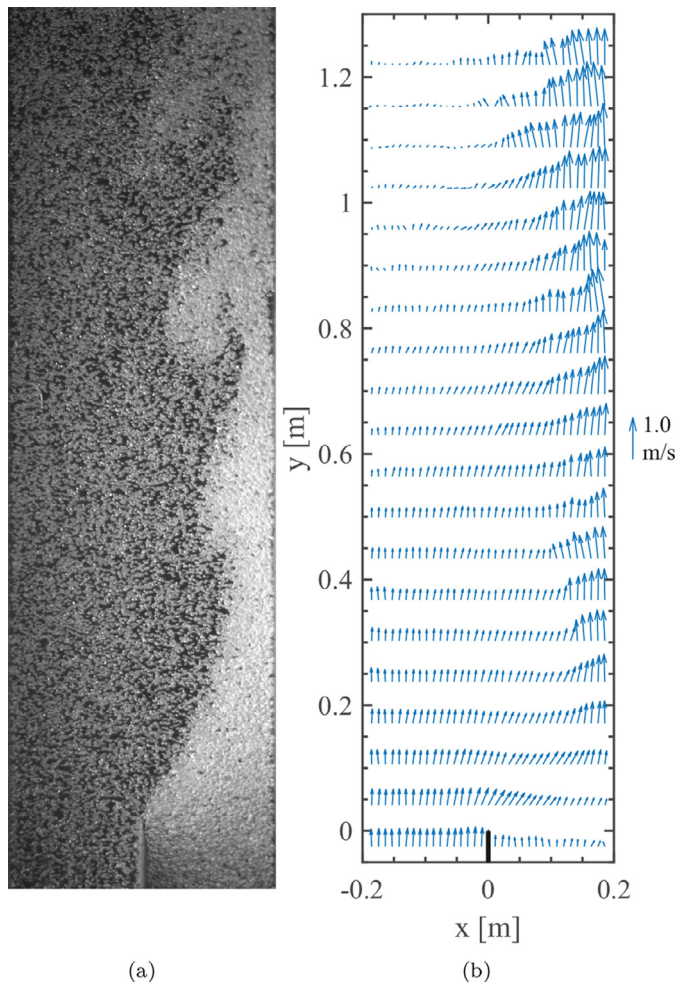


**Fig. 1.** (a) Raw image corrected for lens distortion. (b) Bubble parcel velocity vectors as calculated using Bubble Image Velocimetry (see Part I). Reference vector (1 m/s) given on the right. Average of 5 image pairs,  $\approx 40$  ms. Inlet conditions:  $U_{sg,L} = 0.63$  cm/s;  $U_{sg,R} = 1.87$  cm/s; hence  $\langle U_{sg} \rangle = 1.25$  cm/s and  $\lambda_g = 1$ .  $U_{sl,L} = 0.2$  cm/s;  $U_{sl,R} = 0$  cm; hence  $\langle U_{sl} \rangle = 0.1$  m/s; and  $\lambda_l = -2$ .

The mean superficial gas velocity  $\langle U_{sg} \rangle$  was kept at a value of 1.25 cm/s (unless otherwise mentioned), while  $\lambda_g$  was varied between -1 and 1. Therefore, the superficial gas velocity of each inlet (L,R) was in the range 0.63-1.88 cm/s, which is in the regime where bubbles are formed individually with a very uniform bubble size [Muilwijk and Van den Akker (2019b)]. The mean superficial liquid velocity  $\langle U_{sl} \rangle$  was varied between 0-0.2 m/s. The degree of a-symmetry of the liquid co-flow  $\lambda_l$  was varied between 0, -1, and -2, the latter indicating no liquid flow at the right inlet and  $U_{sl,L} = 2\langle U_{sl} \rangle$ .

More details on the design of the test facility can be found in our previous paper [Muilwijk and Van den Akker (2019b)], where correlations were developed to describe the bubble diameter  $d_b$  and (overall) gas hold-up as a function of the applied superficial liquid and gas velocities. Local gas fractions, bubble velocities and chord lengths for uniform gas sparging and liquid co-flow were reported in Part I for superficial gas velocities in the range 0.63-6.25 cm/s and liquid velocities up to 0.2 m/s. Since we found that Bubble Image Velocimetry can only be applied for low to moderate void fractions, we limit ourselves to show organized flow structures at relatively low  $\langle U_{sg} \rangle$ , such that the assumption of a 2D flow pattern is plausible.

Exploratory bubble streak line experiments were performed in order to investigate the various types of flow patterns as a function

of  $\langle U_{sl} \rangle$ , and the degrees of a-symmetry  $\lambda_g$  and  $\lambda_l$ . Bubble streak-lines were captured (Jai Go 2400M camera, Kowa LMVZ166HC 16-64 mm varifocal lens) for various operating conditions using a focal length of  $\approx 25$  mm  $f/5.4$  and an exposure time of  $1/10$  s and shown in Figs. 2, 8. We found that the bubble velocities at a height of  $\approx 50$  cm above the trailing edge of the splitter plate show mostly uni-directional flow behavior. Part I of this paper showed that at the gas fraction and bubble velocities at  $x = \pm 15$  cm are very much representative for the bulk of the bubble column, where  $x$  is the horizontal coordinate, with  $x = 0$  being the center of the column (see Fig. 1b). So here, we kept the dual-tip optical fibre probes at a fixed position of  $y = 63$  cm above the trailing edge of the splitter plate (80 cm above the gas sparger level) and 5 cm from the column side walls ( $x = \pm 15$  cm). The main reason for measuring gas fractions, bubble velocities, and chord lengths at these positions is that the bubbles move in a mostly vertical direction, aligned with the optical fibre probes. Measuring the hydrodynamic parameters at these locations make the Optical Fibre Probe measurements most reliable. Measuring at lower elevations would miss substantial numbers of bubbles. Measurements with the OFPs were taken for a duration of 300 s to obtain the mean gas fraction and its standard deviation over 30 second intervals as well as bubble velocity and chord length distributions. Series of bubble velocity and chord length measurements were rejected when the pairing rate dropped below 25% as a result of the occurrence of down flowing bubbles. Mean bubble velocities are calculated as the gas fraction weighted mean bubble velocity, see Part I of this paper.

A Bubble Image Velocimetry (BIV) technique, as explained in Part I, was adopted to calculate bubble parcel velocities and to quantify global flow structures. For this part, images were captured of the bubble column for 10 s at a rate of 120 Hz and a spatial resolution of  $\approx 0.7$  mm/pix. The size of an interrogation window was reduced to  $32 \times 32$  pixels to obtain a higher spatial resolution to better capture high gradients in the high shear regions. Fig. 1b shows a vector plot of the ( $5/120$  s average) bubble parcel velocity as calculated using BIV for the case shown in Fig. 1a.

Contour plots of the parcel velocity magnitude, calculated according to:

$$|\bar{v}_b| = \sqrt{v_{b,x}^2 + v_{b,y}^2} \quad (7)$$

and bubble traces were obtained by integrating the mean bubble parcel velocities. The root-mean-square bubble velocity fluctuations were calculated according to:

$$v'_b = \sqrt{v_{b,x}^2 + v_{b,y}^2} \quad (8)$$

where  $v'_{b,i}$  is the instantaneous velocity fluctuation ( $i = x, y$ ).

### 3. Uniform liquid co-flow at a-symmetric air sparging

#### 3.1. The boundary layer between the two bubbly streams

Fig. 2 shows the influence of a uniform liquid co-flow on the flow patterns inside the column. The middle column ( $\lambda_g = 0$ ) shows bubble streaks for uniform aeration with increasing liquid co-flow from the top to the bottom, where  $\langle U_{sl} \rangle = 0$  m/s (top);  $\langle U_{sl} \rangle = 0.1$  m/s (middle); and  $\langle U_{sl} \rangle = 0.2$  m/s (bottom row).

The left ( $\lambda_g = -0.75$ ) and right ( $\lambda_g = 0.75$ ) columns of Fig. 2, with their a-symmetric air sparging, show strong buoyancy driven flow structures at the side with the highest gas fraction (which shows up lighter). The developing boundary between the two bubbly flows of different densities is clearly visible. In all three rows of Fig. 2, the flow fields for  $\lambda_g = -0.75$  and  $\lambda_g = 0.75$  are each other's reflection.

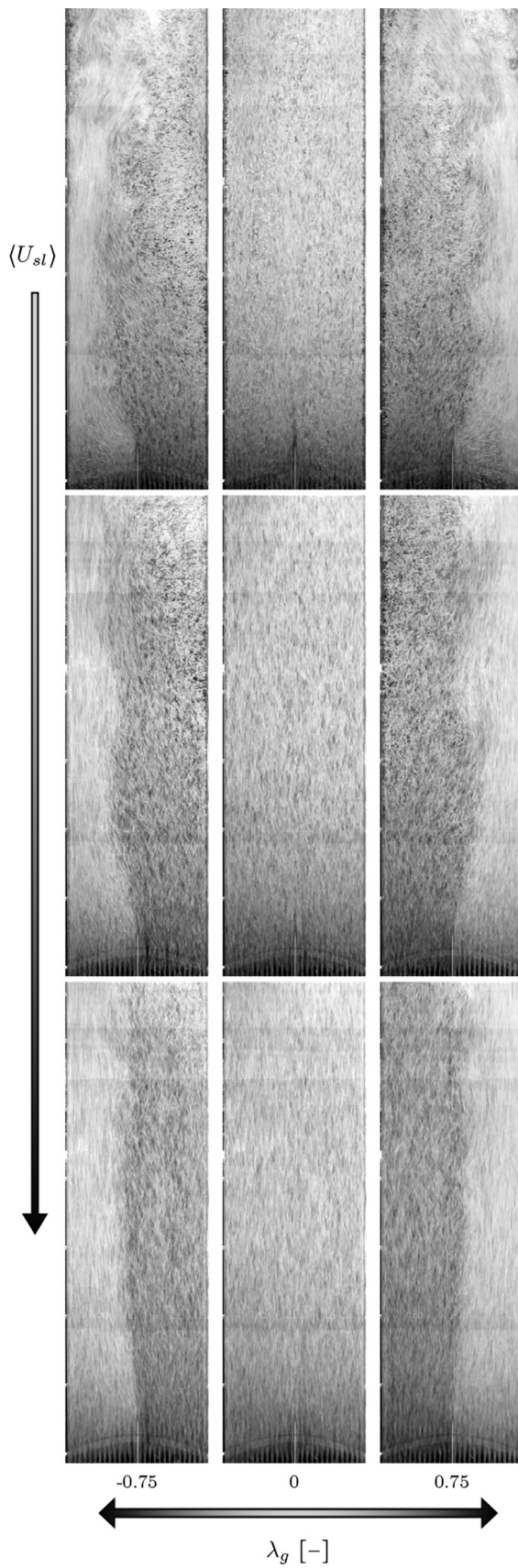


**Fig. 2.** Bubble streaklines for  $\langle U_{sg} \rangle = 1.17$  cm/s. From left to right: varying the degree of a-symmetric gas sparging  $\lambda_g$ . From top to bottom: increasing liquid co-flow velocity (uniform).  $\langle U_{sl} \rangle = 0, 0.1, 0.2$  m/s.  $\lambda_l = 0$ .

In the absence of a liquid co-flow (top row), the liquid carried upwards in the buoyant plume returns on the other side, thereby creating highly unsteady recirculation vortices. The buoyant plume accelerated with increasing height and deflected from the column wall at a height of  $\approx 1$  m above the edge of the splitter plate, whereafter the plane shear layer disappeared by disintegrating into a 3D chaotic turmoil.

A liquid co-flow was found to organize the vortical structures, thereby preserving a quasi-2D shear layer. At a liquid co-flow of 0.1 m/s (middle row), a somewhat more organized vortex appeared higher in the column, while a recirculatory flow was not observed for  $\langle U_{sl} \rangle = 0.2$  m/s (bottom row). Also, the fluctuations of the boundary dampened with increasing liquid co-flow, while the "angle of departure", the development of the lateral position of the boundary, became smaller with increasing co-flow velocity.

The cases with  $\lambda_g \neq 0$  all show unstable (wavy) interfaces between the two bubbly flows. It seems that mainly in the absence of liquid co-flow K-H instabilities are able to grow into well-defined rollup vortices. Obviously, a (stronger) co-flow has a stabilizing effect. It is known from single-phase K-H theory that a Richardson number, denoting the ratio of a velocity difference squared and a difference in specific weight between the parallel flows, governs the formation of K-H instabilities. The complex interplay between flow rates and (local) void fraction impedes a more detailed forecast of the occurrence of such vortices.

### 3.2. Global flow patterns

Fig. 3 shows contour plots of the mean (10s) bubble velocity magnitude obtained by means of BIV. The (uniform) superficial liquid velocity is  $\langle U_{sl} \rangle = 0$  (top); 0.1 (middle); and 0.2 m/s (bottom rows), while the degree of a-symmetric gas sparging is  $\lambda_g = -1$  (left);  $\lambda_g = 0$  (center); and  $\lambda_g = 1$  (right).

The middle columns show almost uniform bubble velocities (Figs. 3b, 3e and 3h) and velocity fluctuations (Figs. 4b, 4e and 4h), where the bubble velocities increase with increasing liquid co-flow velocity (top to bottom), while the velocity fluctuations decrease with increasing  $\langle U_{sl} \rangle$ , which confirms the calming effect of a liquid co-flow as shown in Part I.

Some small gradients of  $|\bar{v}_b|$  are visible even when, without liquid co-flow, the aeration rates left and right were set equal (see Fig. 3b). The bubbles from the left inlet accelerated slightly due to a very small inequality of the superficial gas flow rates at the left and right side of the splitter plate (due to the accuracy rating of the Mass Flow Controllers and a slightly off-centered splitter plate [Muilwijk and Van den Akker (2019b)]). A liquid co-flow then had an equalizing effect on the flow, see Figs. 4b, 4e and 4h, and the flow behavior is less sensitive to small variations in  $\lambda_g$ .

The left and right columns in Figs. 3, 4 show velocity magnitude contours and bubble traces (Fig. 3) and velocity fluctuations (Fig. 4) for unevenly sparged configurations ( $\lambda_g = -1$  for the left and 1 for the right columns respectively).

In all 3 rows of Figs. 3 and 4, the flow structures for  $\lambda_g = -1$  and 1 are very similar when mirrored in  $x = 0$ . For all cases with uneven gas sparging, a buoyancy driven flow pattern emerged, where the bubbles migrated horizontally to the side with the highest gas fraction and accelerated in vertical direction. Without liquid co-flow, see Figs. 3a and 3c, bubbles were moving downwards at the side of the lowest gas fraction, indicating a strong liquid recirculation loop as a result of liquid entrainment in the buoyant plume and mass conservation.

With increasing liquid co-flow rates, bubbles migrated horizontally to a lesser extent, hence, the developing boundary remained more centered in the column and a bubble recirculation loop did not emerge in the field of view up to  $y = 1.2$  m.

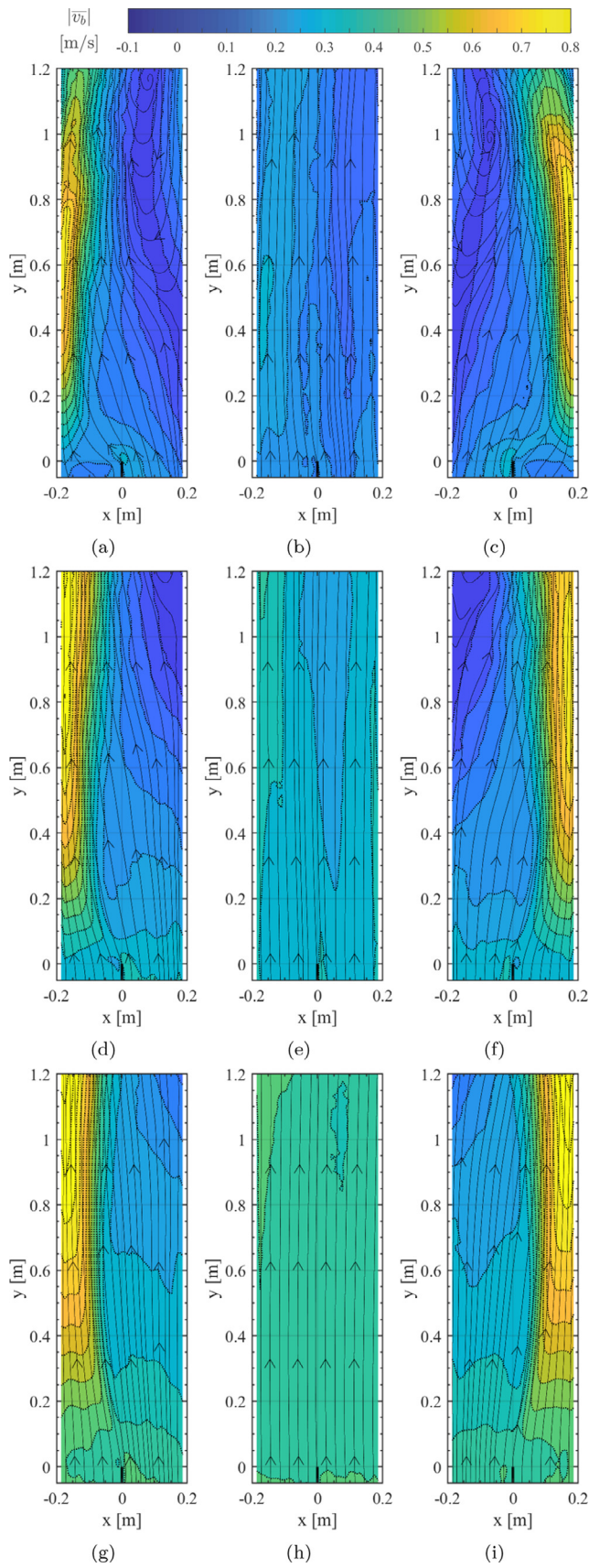


**Fig. 3.** Bubble traces and contours of the velocity magnitude, see Eq. (7), with a uniform co-flow. From left to right:  $\lambda_g = -1, 0, 1$ ; From top to bottom:  $\langle U_{sl} \rangle = 0, 0.1, 0.2$  m/s.  $\langle U_{sg} \rangle = 1.25$  cm/s.

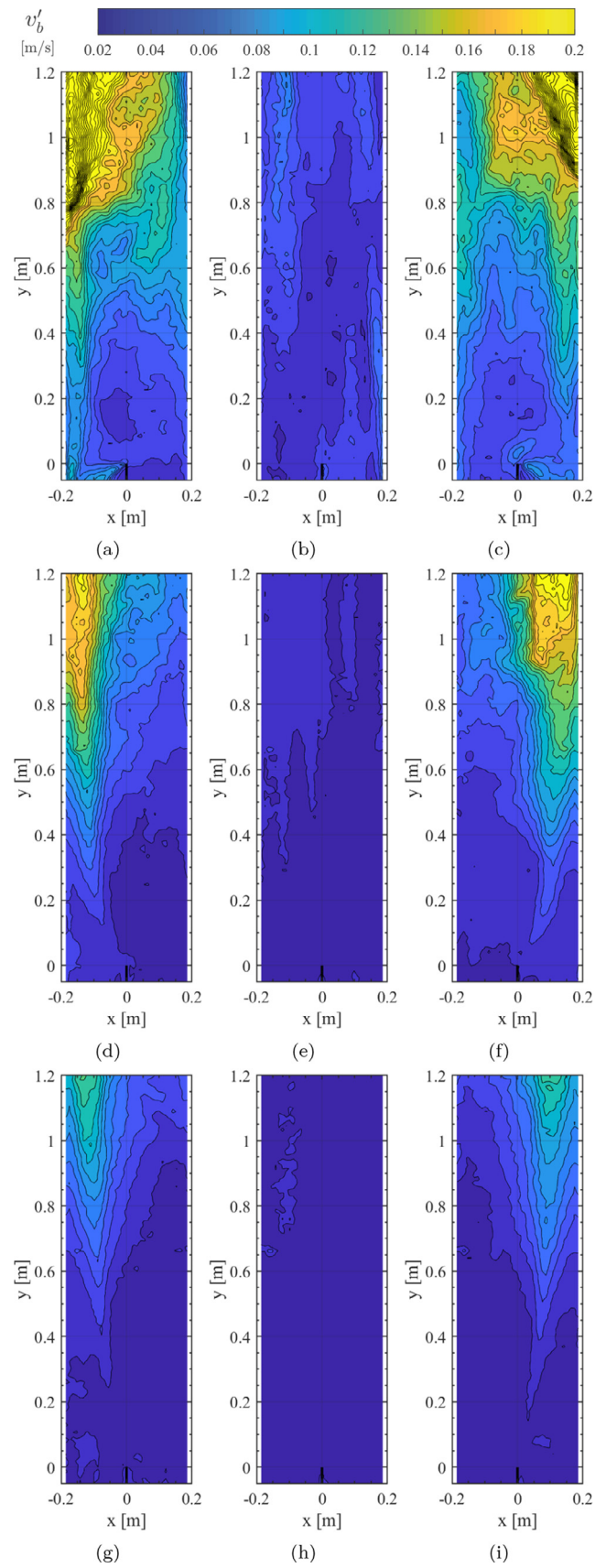


**Fig. 4.** Contour plots of the root-mean-square velocity fluctuations as calculated according to Eq. (8).  $\lambda_g = -1, 0, 1$ ; From top to bottom:  $\langle U_{sl} \rangle = 0, 0.1, 0.2$  m/s.  $\langle U_{sg} \rangle = 1.25$  cm/s.

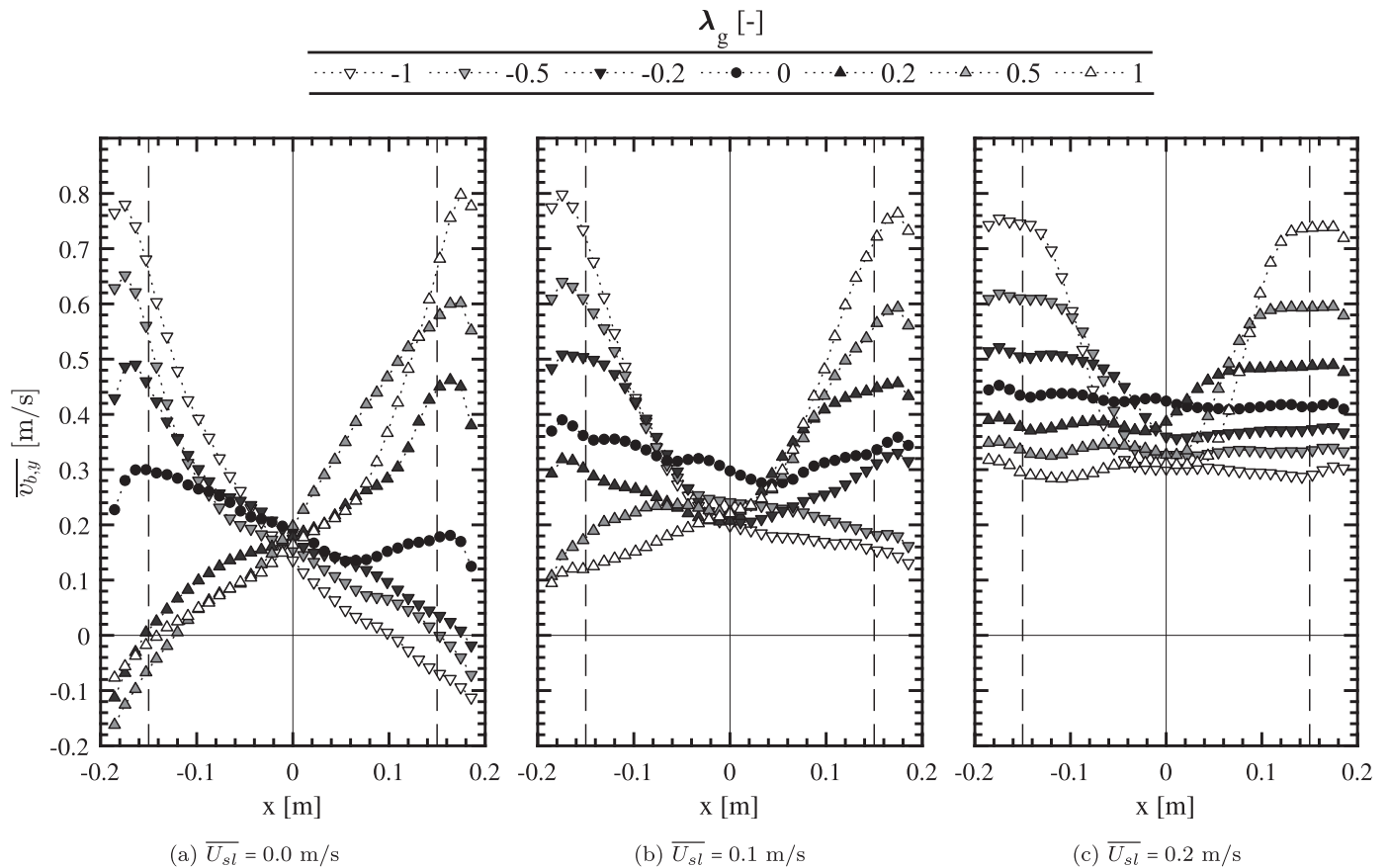


**Fig. 5.** Parcel velocity profiles obtained by BIV measurements at  $y = 63$  cm for various  $\lambda_g$ . From left to right: increasing liquid co-flow velocity (uniform;  $\lambda_l = 0$ ). The dashed lines at  $x = \pm 0.15$  m denote the OFP locations. The velocity profiles in (a) are extracted from Figs. 3a-3c; those in (b) from Figs. 3d-3f; and those in (c) from Figs. 3g-3i for  $\lambda_g = -1, 0, 1$  respectively.

The organizing effect of a liquid co-flow on the flow pattern is evident from the velocity fluctuation contours shown in Fig. 4. Without liquid co-flow and non-uniform gas sparging, (Figs. 4a and 4c), very strong fluctuations were found in the top corners of the column. As the velocity gradients increased with height, the bubble plume detached from the column wall at  $y \approx 1$  m, and the 2-D plane shear layer disintegrated into chaotic 3-D swirling structures. Similar behavior was observed by Alméras et al. (2018), where an inhomogeneously sparged rectangular bubble column was operated in a regime with a planar (2D) recirculation vortex at small gas volume fraction differences:  $\Delta\alpha/\langle\alpha\rangle < 0.4$ .

A uniform liquid co-flow controlled the development of the boundary, organized the flow patterns and a 2-D plane shear layer was preserved. Due to the high gradients of  $\alpha$  at the boundary, some organized vortex-roll up occurred between the high and low  $\alpha$  layer (see right column of Fig. 2), which explains the developing contours (width and intensity) of the velocity fluctuations at the location of the boundary.

### 3.3. Parcel velocity profiles

Fig. 5 shows velocity profiles of the mean vertical parcel velocities ( $y$ -direction), as measured by BIV over a 10 s interval, at a height of  $y = 63$  cm above the trailing edge of the splitter plate. The uniform liquid co-flow velocity ( $\langle U_{sl} \rangle$ ) was fixed at 0.0 m/s (a), 0.1 m/s (b), and 0.2 m/s (c), while the degree of a-symmetric sparging  $\lambda_g$  was varied in the range  $-1..1$  (see legend), with  $\lambda_g = 0$  indicating equal superficial gas flow rates at the left and right inlet. The smooth curves in Fig. 5 illustrate that the image correlation al-

gorithm for calculating parcel velocities, which is described in Part I, works rather well.

For  $\lambda_g < 0$  ( $\nabla, U_{sg,L} > U_{sg,R}$ ), a plume of high bubble velocities developed at the left hand side of the column. A buoyancy driven acceleration occurs of the bubbly stream that has initially a higher gas fraction at the left inlet. When  $\lambda_g > 0$  ( $\Delta, U_{sg,L} < U_{sg,R}$ ), this buoyancy driven bubble plume developed at the right hand side of the column.

In cases with  $\langle U_{sl} \rangle = 0$  m/s, see Fig. 5a, a global liquid circulation was established due to the absence of a net liquid through flow. This rather unsteady vortex dragged down bubbles at the side of the lowest  $U_{sg}$ , see also the top left and right bubble streaks in Fig. 2. Due to the wandering behaviour of the bubble plume, vortices were generated at the free interface that traveled down the column. Low frequency flow instabilities caused this 2D flow pattern to disintegrate into a chaotic turmoil at some 1 meter above the trailing edge of the splitter plate, see also the contour plots in Figs. 4a and 4c. Therefore, it should be noted that the velocity profiles are a 10 s average and different velocity profiles may be measured for different time intervals and further study is required to study the dynamics of the column.

With increasing  $\langle U_{sl} \rangle$ , see Figs. 5b and 5c, the development of a liquid recirculation loop was inhibited due to advection of bubbles. Liquid co-flow had a stabilizing and organizing effect on the flow patterns and low frequency instabilities for cases with  $\langle U_{sl} \rangle = 0$  m/s were removed. For the highest  $\langle U_{sl} \rangle$  setting (5c), almost flat velocity profiles were measured at both sides (left, right) of the boundaries where velocity gradients occurred. As the bubbly stream with the highest/lowest initial gas fraction acceler-

$\langle U_{sl} \rangle$ [m/s]	0	0.1	0.2	
$x$	-15	◁	◄	◀
[cm]	15	▷	►	▶

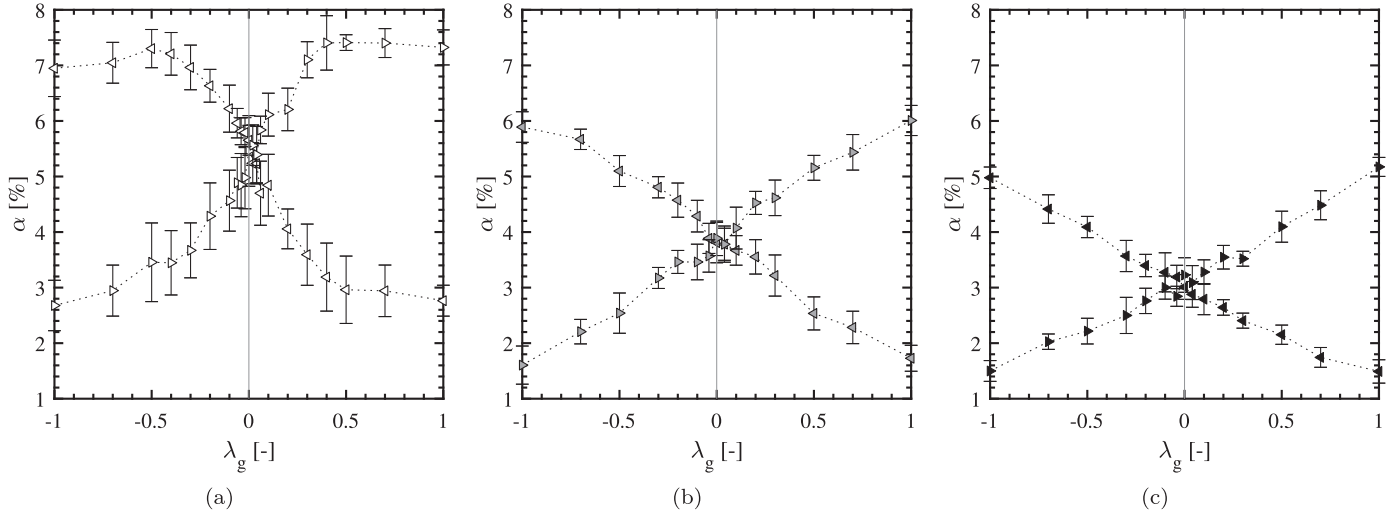


**Fig. 6.** The void fraction  $\alpha$  at  $x = \pm 15$  cm and  $y = 63$  cm as a function of the degree of asymmetry  $\lambda_g$ . ( $U_{sg}$ )=1.25 cm/s. (a)  $\langle U_{sl} \rangle = 0$  m/s; (b)  $\langle U_{sl} \rangle = 0.1$  m/s; and (c)  $\langle U_{sl} \rangle = 0.2$  m/s. The error bars indicate the standard deviation over 30 s intervals.

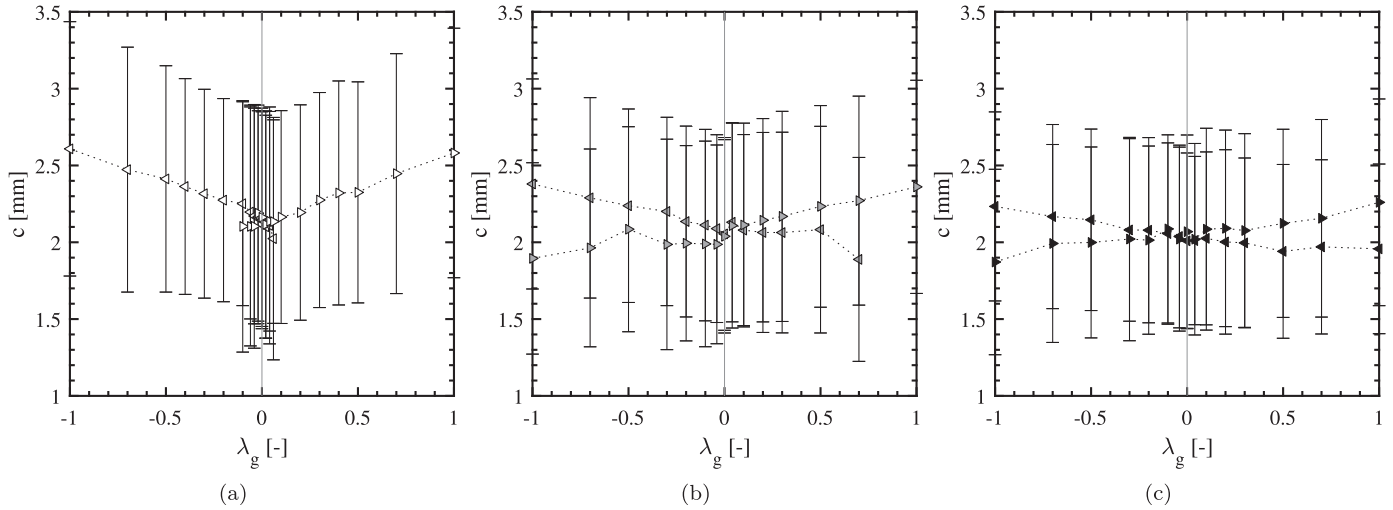


**Fig. 7.**  $\bar{c}$  at  $x = \pm 15$  cm and  $y = 63$  cm as a function of the degree of asymmetry  $\lambda_g$ . ( $U_{sg}$ )=1.25 cm/s. (a)  $\langle U_{sl} \rangle = 0$  m/s; (b)  $\langle U_{sl} \rangle = 0.1$  m/s; and (c)  $\langle U_{sl} \rangle = 0.2$  m/s. The error bars indicate the standard deviation of the chord length distributions. See also legend of Fig. 6.

ated/decelerated with the flow direction respectively, the velocity difference between the left and right plateau increased, see also Figs. 3g and 3i. With increasing/decreasing  $\lambda_g$ , departing from 0, the boundary layers drifted more to the right/left side respectively, while thickness of the boundary decreased with  $|\lambda_g|$ .

In the ideal case of symmetric gas sparging, a flat bubble velocity profile is expected. Due to slight inaccuracies of the Mass Flow Controllers, the left side of the column received a higher gas flux at  $\lambda_g = 0$ . The development of the bubble velocity profiles was found to be highly sensitive to slight changes in  $\lambda_g$  in the absence of a liquid co-flow, see • in Fig. 5a. This effect is largely reduced in the effect of a liquid co-flow velocity, see Figs. 5b and 5c.

The dashed lines at  $x = \pm 0.15$  m indicate the locations (at  $y = 63$  cm) of the optical fibre probes. The results thereof are discussed below.

### 3.4. Local flow measurements

#### 3.4.1. Gas fraction

Fig. 6 shows the development of the gas fraction  $\alpha$  at  $y = 63$  cm and  $x = -15$  cm and  $x = 15$  cm as a function of the degree of a-symmetric gas sparging  $\lambda_g$  for (a)  $\langle U_{sl} \rangle = 0$  (open markers); (b)  $\langle U_{sl} \rangle = 0.1$  (grey markers); and (c)  $\langle U_{sl} \rangle = 0.2$  m/s (black markers). For each  $\lambda_g$ , the measurement at  $x = -15$  ( $\triangleleft$ ) and  $x = +15$  cm ( $\triangleright$ ) were taken simultaneously for a duration of 300 s.

The highest gas fraction was obtained at the side with the highest superficial gas velocity; on the left side when  $\lambda_g < 0$  and on the right side when  $\lambda_g > 0$ . The markers on the left (at  $\lambda_g = -1$ ), correspond to the cases shown in the left column of Figs. 3, 4, whereas the markers on the right ( $\lambda_g = 1$ ) resemble the cases as shown in the right columns of Figs. 3, 4. Therefore, the evolution

of  $\alpha$  (at the measurement locations) with respect to  $\lambda_g$  is almost symmetric in  $\lambda_g = 0$ .

For  $\langle U_{sl} \rangle = 0$  (open markers), the line of symmetry (where the gas fractions at  $x = -15$ ,  $\triangleleft$ , and  $x = +15$  cm,  $\triangleright$ , are equal), is found slightly right of  $\lambda_g = 0$ . This agrees well with our earlier observation that the calibration of the mass flow controllers is slightly different (yet still within the specifications), as symmetry was obtained when  $\lambda_g \approx 0.02$ . A liquid co-flow then mitigated the effect of a slight imbalance between both superficial gas velocities (Left/Right) as the curves for  $\langle U_{sl} \rangle = 0.1$  and  $0.2$  m/s seem to be very symmetric around  $\lambda_g = 0$ .

For  $\langle U_{sl} \rangle = 0.2$  m/s (black markers), the two gas fractions vary almost linearly with  $\lambda_g$  in the whole range  $\lambda_g = -1 \dots 1$ , whereas for  $\langle U_{sl} \rangle = 0$  m/s,  $\alpha$  was very sensitive to  $\lambda_g$  in the range  $-0.3 \dots 0.3$ , followed by a plateau for  $|\lambda_g| > 0.4$ . As the width of the bubble plume decreases with increasing  $\lambda_g$  and  $y$ , the (average) boundary surpasses  $x = \pm 15$  cm (see Fig. 3a, 3c), such that the optical probes at the high  $U_{sg}$  side also encountered bubbles originated at the low  $U_{sg}$  side. Hence, the gas fraction as a function of  $\lambda_g$  leveled off at high  $|\lambda_g|$  as the void fraction maximum emerged closer to the column side walls.

Without liquid co-flow, see Fig. 6a, a steep gradient of  $\alpha$  with respect to  $\lambda_g$  was found close to  $\lambda_g = 0$ , indicating that the overall flow behavior is very sensitive to small differences of the superficial gas velocities between the left and right inlet and strong buoyancy driven flow structures emerged. With liquid co-flow, see Figs. 6b, 6c, the steep gradient close to  $\lambda_g = 0$  disappears as the flow stabilizes and aligns more vertically.

### 3.4.2. Bubble velocities

The detailed velocity data of individual bubbles are presented separately in the Appendix as they may be useful for validation of CFD simulations. A.1 shows a comparison between vertical parcel velocities  $\bar{v}_{b,y}$  and bubble velocities measured by the OFPs.

### 3.4.3. Bubble chord lengths

Fig. 7 shows the mean chord length  $\bar{c}$  at  $x = \pm 15$  cm and  $y = 63$  cm as a function of the degree of a-symmetric gas sparging  $\lambda_g$  for the same cases as outlined in Fig. 6. Bubbles were formed separately (one-by-one) and, for each of the inlets (L,R), a very uniform bubble size can be assumed for cases with a low  $U_{sg}$  such as studied in this paper (see Muilwijk and Van den Akker (2019b)).

As, however, the bubble size formed in each of the inlet sections (L,R) depends on the applied  $U_{sg}$  and  $U_{sl}$ , an overall bi-modal bubble size distribution was created when  $|\lambda_g| > 0$ , where the larger bubbles were formed in the stream with the highest  $U_{sg}$ .

Mean bubble chord lengths were measured in the range 1.9–2.4 mm for  $\langle U_{sl} \rangle = 0.1 - 0.2$  m/s, where the difference of  $\bar{c}$  between  $x = -15$  and  $x = 15$  cm decreased with increasing  $\langle U_{sl} \rangle$ . For  $\langle U_{sl} \rangle = 0$  m/s, no data could be obtained when the bubble velocities were not upwards or not vertically aligned with the probes. Bubble chord lengths were found in the range 2.1–2.6 mm for the side with the highest aeration rate ( $x = -15$  cm when  $\lambda_g < 0$  and  $x = 15$  cm when  $\lambda_g > 0$ ).

The width of the chord length distribution for this set of experiments was found to be almost independent of  $\lambda_g$  and decreasing with  $\langle U_{sl} \rangle$ .

## 4. Non-uniform liquid co-flow at a-symmetric air sparging

### 4.1. The boundary layer between the two bubbly streams

Fig. 8 shows, in addition to the effect of a-symmetric gas sparging as in Fig. 2, also the influence of an a-symmetric liquid co-flow on the flow patterns inside the column.

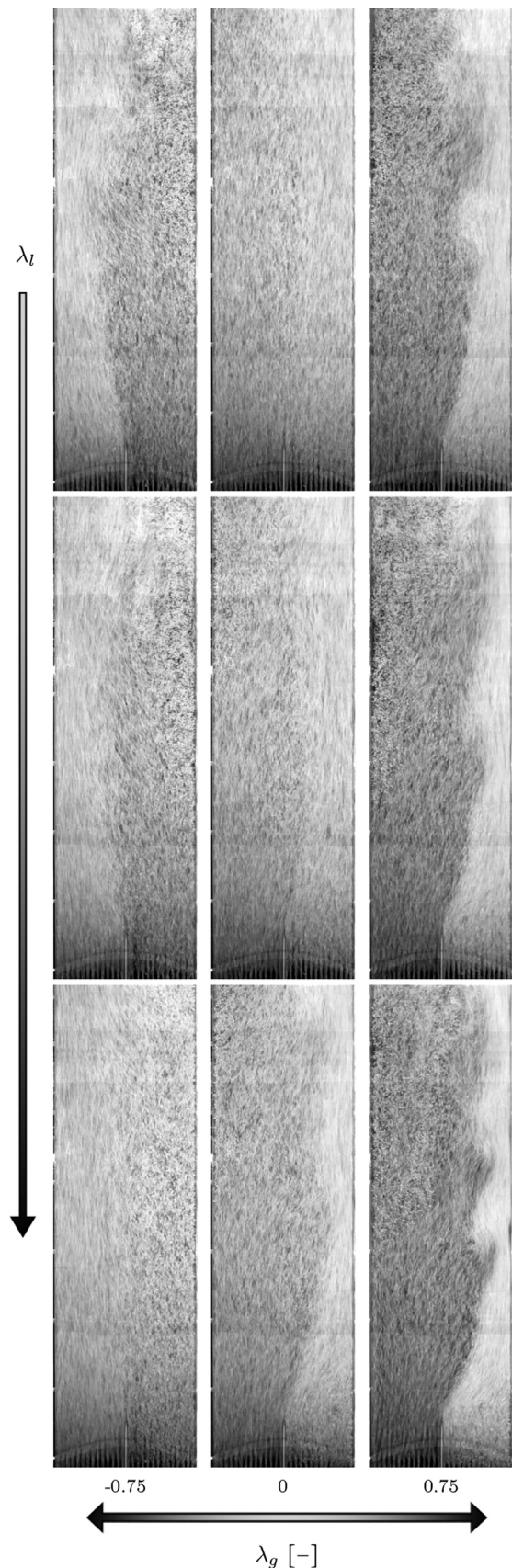


**Fig. 8.** Bubble streaklines for  $\langle U_{sg} \rangle = 1.17$  cm/s and  $\langle U_{sl} \rangle = 0.1$  m/s. From left to right: varying the degree of a-symmetric gas sparging  $\lambda_g$ . From top to bottom: increasing degree of a-symmetric liquid co-flow,  $\lambda_l = -0.5, -1, -2$  (high liquid co-flow at the left inlet).

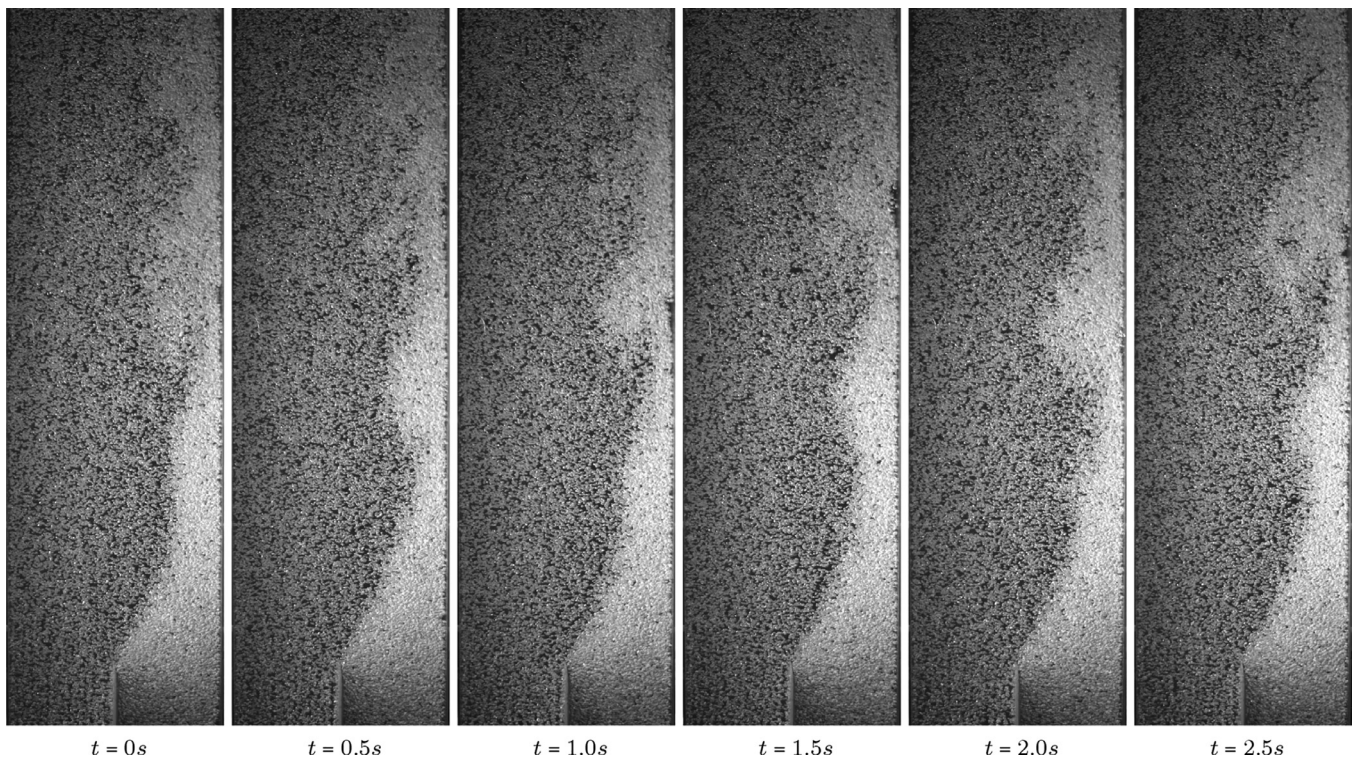


**Fig. 9.** Photographs of a vortex roll-up phenomenon. The time between each frame is 0.5 s. See Supplementary Material online for the embedded video.  $U_{sg,L} = 0.81$  cm/s;  $U_{sg,R} = 1.69$  cm/s;  $\lambda_g = 0.7$ ;  $U_{sl,L} = 0.2$  m/s;  $U_{sl,R} = 0$  m/s;  $\lambda_l = -2$ ;

The middle column ( $\lambda_g = 0$ ) shows bubble streaks for uniform aeration. While the mean liquid co-flow velocity ( $\langle U_{sl} \rangle$ ), see Eq. (2) was kept at 0.1 m/s, the difference of liquid co-flow between the left and right inlet increases from the top to the bottom row of Fig. 8. The degree of a-symmetry for the liquid co-flow ( $\lambda_l$ ) was varied between -0.5 (top); -1 (middle); and -2 (bottom row), with the left side inlet having the highest liquid co-flow velocity and  $\Delta U_{sl} < 0$ , see Eq. (4). Therefore, all  $\lambda_l$  values are negative in the presented configurations. For the bottom case, where  $\lambda_l = -2$ , there was no liquid flow at the right inlet ( $U_{sl,R} = 0$ ), while  $U_{sl,L} = 0.2$  m/s. As the bubbly flow on the left has the lowest gas fraction (due to the higher  $U_{sl}$ ), the boundary develops to the right side due to the buoyancy driven acceleration of the stream with the highest gas fraction.

For the left column, where  $\lambda_g = -0.75$  (high gas flow left), the boundary evolved to the center (from the top case to the bottom case) as the gas fraction difference decreased from the top row to the bottom row of the figure, hence, less-to-none buoyancy-driven flow patterns were caused for  $\lambda_g = -0.75$  and  $\lambda_l = -2$  at  $\langle U_{sl} \rangle = 0.1$  m/s.

Very unstable boundaries were observed for the cases shown in the right column of Fig. 8, where the highest gas fraction is at the low liquid velocity side. The boundary consistently gravitated towards the side with the highest gas fraction and significantly larger angles of departure were observed compared to the other cases shown in Figs. 2, 8. A Kelvin-Helmoltz type of flow instability seemed to occur only in extreme cases and a clear visible vortex roll-up was visible in the bubble streaks for  $\lambda_g = 0.75$  and  $\lambda_l = -2$ .

Fig. 9 shows photographs ( $1/400$  s) of the bubble column for a which a repeating vortex roll-up flow pattern was observed ( $\langle U_{sg} \rangle = 1.25$  cm/s;  $\lambda_g = 0.70$ ;  $\langle U_{sl} \rangle = 0.1$  m/s; and  $\lambda_l = -2$ ). The time between each photograph is 0.5 s. As evident from the bubble streaks shown in Fig. 8, this large vortex roll-up only occurs for very specific conditions. The frequency of vortex formation and

movement of the vortex core is clearly visible and the period is estimated at  $\approx 1.5$  s. Exploratory experiments reveal that this frequency depends on  $\lambda_g$  and  $\lambda_l$ , but more experiments are required for extended periods of time to obtain a sufficient resolution in the frequency domain (when calculating a fast Fourier Transform of the boundary location or bubble density at a monitoring location). As the bubble detection frequency by the OFPs is low compared to the frequency of the oscillation as visualized in Fig. 9, (spectral) analysis of the phase indicator function or bubble velocity did not yet yield meaningful results.

An advanced image analysis technique (boundary detection or spectral analysis of the local bubble density) may be useful to construct a regime map of operating conditions for which this type of organized periodic flow behavior emerges.

#### 4.2. Global flow patterns

Fig. 10 shows contours of the mean bubble velocity magnitude and bubble traces for  $\lambda_g = -1, 0, 1$  (from left to right) and  $\lambda_l = -1$  (top) and -2 (bottom), whereas Fig. 11 shows contours of the fluctuating velocity in a similar arrangement. The mean superficial liquid velocity ( $\langle U_{sl} \rangle = 0.1$  m/s). Hence, the conditions are comparable to those of which the bubble streaks are given in the second and third row of Fig. 8. Figs. 12, and 13 are similar to Figs. 10 and 11, but for  $\langle U_{sl} \rangle = 0.2$  m/s.

Due to the difference of the liquid co-flow velocity between both inlets (the left inlet having the highest  $U_{sl}$  for all cases shown), flow patterns corresponding to  $\lambda_g = -1$  and 1 are no longer symmetric.

For all cases, the fluid at the side of the highest gas fraction (appears lighter in Fig. 8) accelerated while entraining fluid from the trans-boundary side. If the liquid co-flow velocity was then insufficiently high, global bubble recirculation vortices appeared as presented in the top regions (blue) of Figs. 11a, 11c and 11d, while

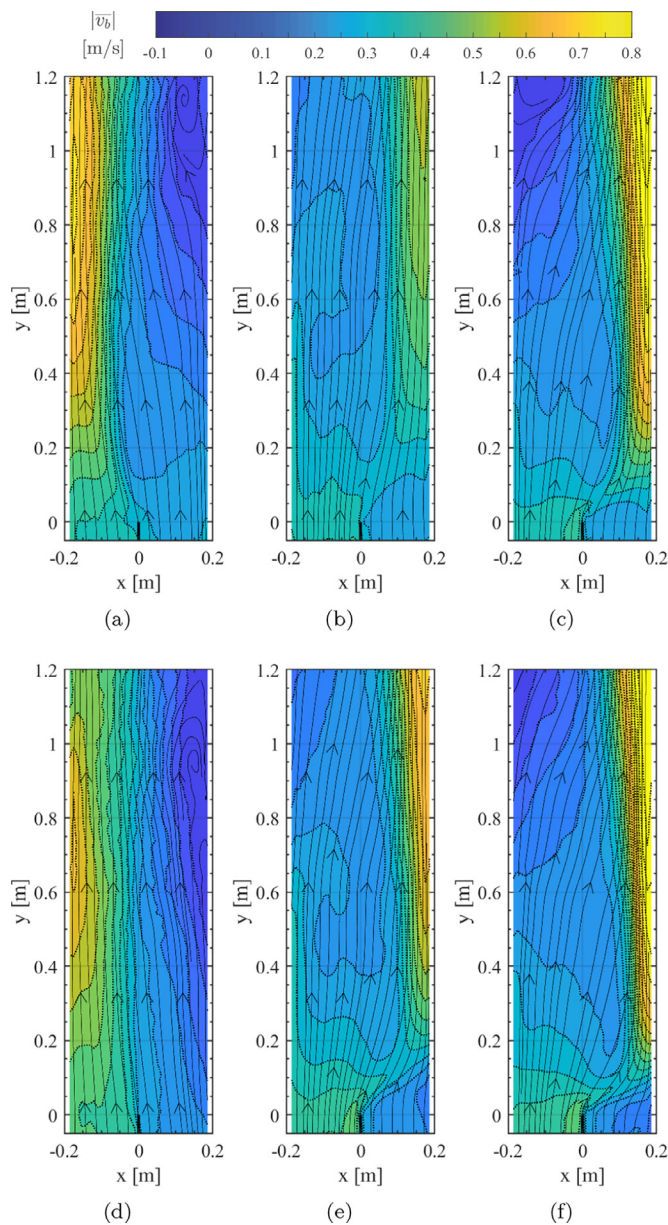


**Fig. 10.** Bubble traces and velocity magnitude contours.  $\langle U_{sg} \rangle = 1.25$  cm/s; from left to right: more gas flow left ( $\lambda_g = -1$ ), even distribution ( $\lambda_g = 0$ ), more gas flow right ( $\lambda_g = 1$ ).  $\langle U_{sl} \rangle = 0.1$  m/s; upper row: more liquid co-flow left ( $\lambda_l = -1$ ); lower row: all liquid co-flow left ( $\lambda_l = -2$ ); see Figs. 3d-3f for uniform co-flow ( $\lambda_l = 0$ ).

no downward moving bubbles were observed when  $\langle U_{sl} \rangle = 0.2$  m/s (Fig. 12). As noticeable from the structures in the contours of the velocity fluctuations, Figs. 11, 13, a liquid co-flow has an organizing effect on the flow pattern. As a liquid co-flow strongly contributed to the momentum flux, emerging buoyancy driven flow structures were more organized, and a 2D flow behavior was sustained for a wider range of  $\lambda_g$  and stream wise locations  $y$ .

We observed vortex roll-up for various conditions at different positions and at different scales. De Tournemine and Roig (2010) (half-sparged configuration) reported oscillating boundaries when bubbles were injected at the high liquid velocity side at the inlet ( $\lambda_g \lambda_l > 0$ ). This agrees well with our experiments depicted in Figs. 12a and 13a (where vortex roll-up occurred at the boundary), but to a lesser extent in Figs. 10a and 11a where the liquid co-flow velocity was lower. In the latter case, a global flow pattern emerged due to a larger influence of buoyancy difference

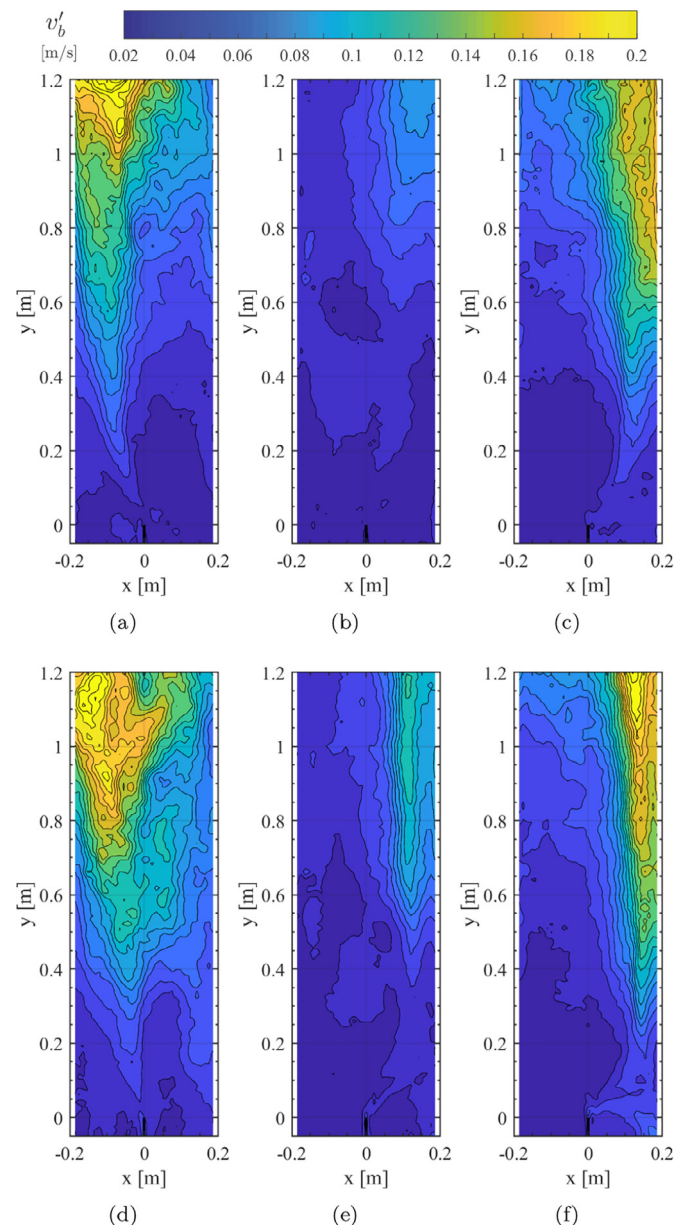


**Fig. 11.** Contour plots of the RMS velocity.  $\langle U_{sg} \rangle = 1.25$  cm/s; from left to right: more gas flow left ( $\lambda_g = -1$ ), even distribution ( $\lambda_g = 0$ ), more gas flow right ( $\lambda_g = 1$ ).  $\langle U_{sl} \rangle = 0.1$  m/s; upper row: more liquid co-flow left ( $\lambda_l = -1$ ); lower row: all liquid co-flow left ( $\lambda_l = -2$ ); see Figs. 4d-4f for uniform co-flow ( $\lambda_l = 0$ ).

driven flow pattern. At the opposite end of the spectrum when  $\lambda_g \lambda_l < 0$ , (higher  $U_{sg}$  at the low  $U_{sl}$  side as in Fig. 8 for  $\lambda_g = 0.75$  and  $\lambda_l = -2$ , Figs. 10f and 12f), also unstable boundaries were observed. Large buoyancy driven vortex roll-up structures (of a size significantly larger than  $10\times$  the bubble diameter) were created as shown in Fig. 9 (see also Supplementary Material online), whereas De Tournemine and Roig (2010) reported steady boundaries in this operating regime. This may be due to the lower  $U_{sl}$  and higher  $\alpha$  and larger bubbles in our case, which may trigger flow instabilities.

In specific cases, when the void fraction of both the left and right stream were (exactly) equal, no buoyancy driven flow structures were formed and a mixing layer type of flow pattern was then observed. Fig. 12d shows a case where there is almost no buoyancy driven global flow pattern. While the boundary was hardly detectable (no void fraction difference, which behavior is similar to the case shown in Fig. 8 for  $\lambda_g = -0.75$  and  $\lambda_l = -2$ ),

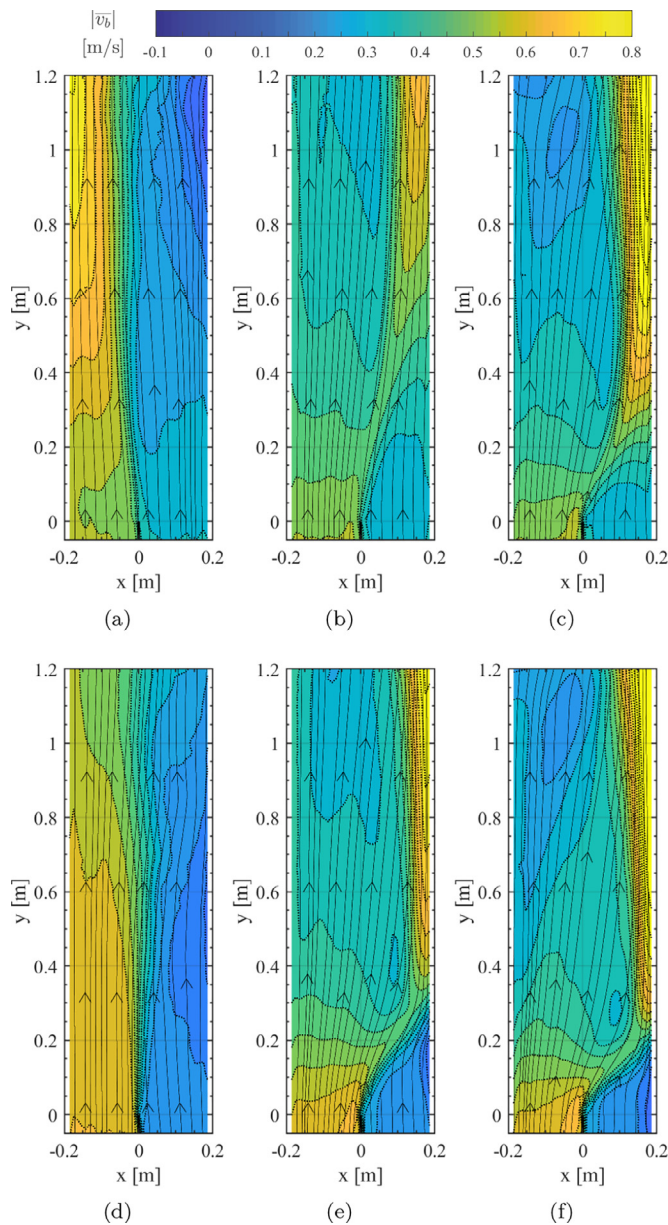


**Fig. 12.** Bubble traces and velocity magnitude contours.  $\langle U_{sg} \rangle = 1.25$  cm/s; from left to right: more gas flow left ( $\lambda_g = -1$ ), even distribution ( $\lambda_g = 0$ ), more gas flow right ( $\lambda_g = 1$ ).  $\langle U_{sl} \rangle = 0.2$  m/s; upper row: more liquid co-flow left ( $\lambda_l = -1$ ); lower row: all liquid co-flow left ( $\lambda_l = -2$ ); see Figs. 3g-i for uniform co-flow ( $\lambda_l = 0$ ). See Supplementary Material online for the videos of (d) and (f).

bubble velocities were very much unidirectional (by inspection of bubble streaks), and the boundary location remained centered (see also the Supplementary Material online for the video of this case). Also, the initial velocities of the left and right inlets, were preserved for a large range of  $y$  (almost no color gradient in vertical direction in the vicinity of the left and right column wall). The contours of the corresponding velocity fluctuations (Fig. 13d) show a very symmetric growth pattern around  $x = 0$ , which indicates that the width of the shear layer increased with height and developed aligned with the splitter plate and a mixing-layer type of flow pattern (see Brown and Roshko (1974)) was recovered. As buoyancy differences were (almost) absent, a liquid-shear driven vortex roll-ups occurred in the center of the bubble column for this specific case, which was found to have smaller structures than the buoyancy-driven vortex roll-up structures.

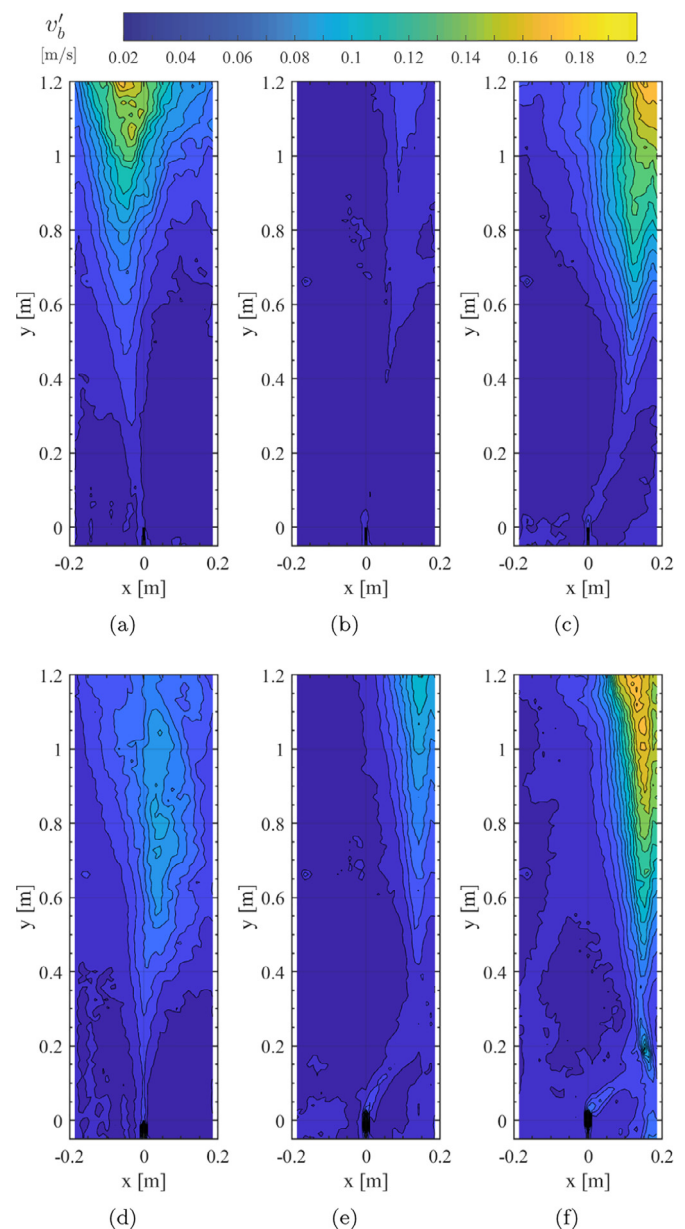


**Fig. 13.** Contour plots of the RMS velocity.  $\langle U_{sg} \rangle = 1.25$  cm/s; from left to right: more gas flow left ( $\lambda_g = -1$ ), even distribution ( $\lambda_g = 0$ ), more gas flow right ( $\lambda_g = 1$ ).  $\langle U_{sl} \rangle = 0.2$  m/s; upper row: more liquid co-flow left ( $\lambda_l = -1$ ); lower row: all liquid co-flow left ( $\lambda_l = -2$ ); see Fig. 4g-i for uniform co-flow ( $\lambda_l = 0$ ).

### 4.3. Parcel velocity profiles

Fig. 14 shows velocity profiles of the mean vertical parcel velocities ( $y$ -direction), as measured by BIV, at a height of  $y = 63$  cm above the trailing edge of the splitter plate. The uniform liquid co-flow velocity  $\langle U_{sl} \rangle$  was fixed at 0.2 m/s and the degree of a-symmetric sparging  $\lambda_g$  was varied in the range  $-1..1$  (see legend). The effect of a-symmetric liquid co-flow is shown in Figs. 14a and 14b for  $\lambda_l$  equal to  $-1$  and  $-2$ , respectively. The latter case represents the case of no liquid co-flow at the right inlet and a superficial liquid velocity of  $2\langle U_{sl} \rangle = 0.4$  m/s for the left inlet.

The reader is referred back to Fig. 5c for  $\lambda_l = 0$  for  $\langle U_{sl} \rangle = 0.2$  m/s. While the velocity profiles Fig. 5c show symmetric behavior around  $x = 0$  m for the various  $\lambda_g$  conditions, velocity profiles in Fig. 14 are no longer symmetric around  $x = 0$  cm, nor  $\lambda_g = 0$  due to the a-symmetric liquid co-flow.

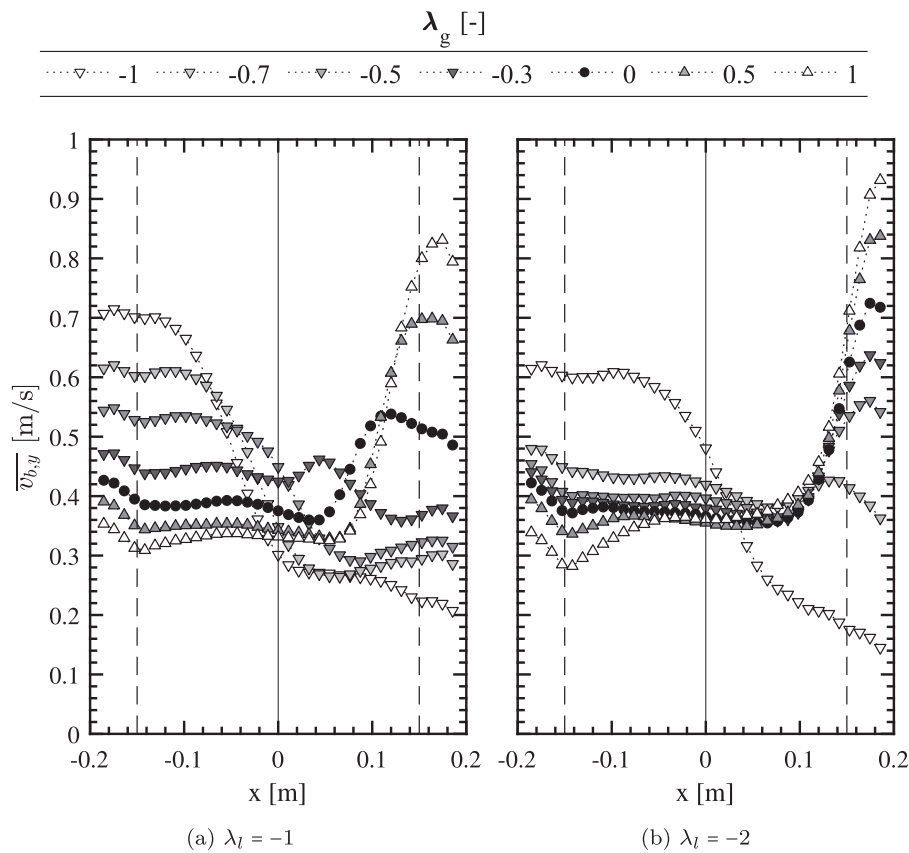


**Fig. 14.** Bubble parcel velocity profiles obtained by BIV measurements at  $y = 63$  cm for various  $\lambda_g$ .  $\langle U_{sl} \rangle = 0.2$  m/s. From left to right: increasing asymmetry of the liquid co-flow,  $\lambda_l$ . The dashed lines at  $x = \pm 0.15$  m denote the OFP locations. The velocity profiles in (a) are extracted from Figs. 12a-12c, and the velocity profiles in (b) are extracted from Figs. 12d-12f for  $\lambda_g = -1, 0, 1$  respectively.

As  $U_{sl,L} > U_{sl,R}$ , the gas fraction of the bubbly stream originating from the left inlet became lower than that from the right inlet for the majority of the cases. Therefore, due to the gas fraction differences, the bubbly stream from the right inlet accelerated and the stream from the left inlet, with an initially higher velocity at  $y = 0$  decelerated, see Figs. 10b, 10c, 10e, 10f and Figs. 12b, 12c, 12d, 12e, 12f.

For some cases, the region with highest bubble velocities remained at the left side. This occurred for  $\lambda_g \leq -0.3$  when  $\lambda_l = -1$  (a) or for  $\lambda_g < -0.7$  when  $\lambda_l = -2$  (b). When the reducing effect of the liquid co-flow on the gas fraction was (over)compensated by a sufficiently high superficial gas velocity ( $U_{sg,L} \gg U_{sg,R}$ ), the resulting gas fraction of the stream from the left inlet was higher than that of the right inlet. This resulted then in a buoyancy driven acceleration of the stream coming from the left inlet.

Around the tipping points,  $\lambda_g \approx -0.3$  for  $\lambda_l = -1$  and especially  $\lambda_g \approx -0.7$  for  $\lambda_l = -2$ , the measured velocity profiles appear very sensitive towards changes in  $\lambda_g$ . For high (positive)  $\lambda_g$ , when the initial gas fraction contrast is high, velocity profiles are becoming less dependent on variations of  $\lambda_g$ . For those cases, the bubbly stream from the right inlet accelerated in a very strong manner, while being pushed even more to the right side due to the high(er) co-flow velocity at the left side. This resulted, partly due the near vicinity of the column right wall, in strong velocity and gas fraction gradients, leading to vortex roll-up behavior as illustrated in Fig. 9.

#### 4.4. Local flow measurements

##### 4.4.1. Gas fraction

Fig. 15 shows the development of  $\alpha$  at  $x = \pm 15$  cm and  $y = 63$  cm as a function of  $\lambda_g$  for  $\lambda_l = 0$  (white markers),  $-1$  (grey mark-

ers) and  $-2$  (black markers) and for (a)  $\langle U_{sl} \rangle = 0.1$  and (b)  $0.2$  m/s. For the sake of comparison, the white markers in Fig. 15a and 15b show the same results as the grey and black markers in Fig. 6 respectively. The triangles pointing right ( $\triangleright$ ) denote measurements taken at  $x = 15$  cm, while the left pointing triangles ( $\triangleleft$ ) represent measurements taken at  $x = -15$  cm.

While the open markers  $\lambda_l = 0$  exhibit a symmetric pattern around  $\lambda_g = 0$ , where the highest gas fraction was measured at the side of the highest aeration rate (left if  $\lambda_g < 0$  and vice versa), symmetry around  $\lambda_g = 0$  was lost for  $\lambda_l \neq 0$ . In extreme cases, for  $\langle U_{sl} \rangle = 0.2$ ,  $\lambda_l = -2$  and  $\lambda_g \geq 0$ , see Fig. 15b and Figs. 12e, 12f, the boundary drifted to the right side in a very strong manner. As the width of the bubble plume became less than or equal to 5 cm, the OFP at  $x = 15$  cm was no longer located solely in the bubble swarm originating from the right inlet, but in the centre of the highly unstable boundary, (where vortex roll-up occurred, see Figs. 13e, 13f). As the bubble plume became thinner with decreasing  $\lambda_l$  and increasing  $\lambda_g$ , the probe at  $x = 15$  cm increasingly dwelled in the trans-boundary side (the bubble swarm originating from the left inlet with a low gas fraction), hence, the gas fraction measured at  $x = 15$  cm (black triangles) no longer increased with increasing  $\lambda_g$ .

Due to an uneven liquid co-flow, the highest gas fraction was not necessarily found at the side of the highest aeration rate. A co-flow affects the (overall) gas fraction according to a correlation developed in our previous paper [Muilwijk and Van den Akker (2019b)] and validated in Part I:

$$\alpha = \frac{U_{sg}}{U_{sg} + U_{sl} + \xi U_t} \quad (9)$$

with  $U_t$  the terminal rise velocity of an isolated bubble ( $\approx 24$  cm/s) and  $\xi \approx 0.82$ . An initial ( $y = 0$ ) gas fraction difference was thus

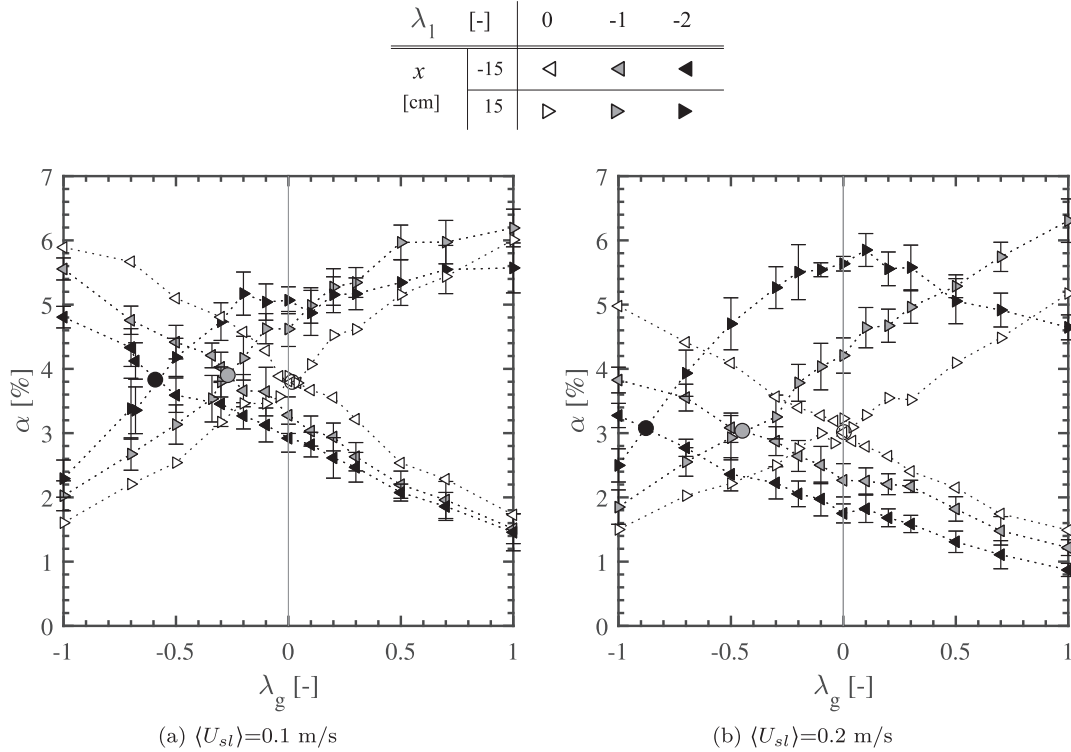


**Fig. 15.**  $\alpha$  as a function of the degree of asymmetry  $\lambda_g$  at  $x = \pm 15$  cm and  $y = 63$  cm for  $\lambda_l = 0$  (from Fig. 6), -1 and -2.  $\langle U_{sg} \rangle = 1.25$  cm/s. The circles show the interpolated operating condition for which  $\alpha_{x=-15} = \alpha_{x=15}$ . The error bars denote the standard deviations based on 30 s intervals.

created for most cases when  $\lambda_g \neq 0$  ( $U_{sg,L} \neq U_{sg,R}$ ) and/or  $\lambda_l \neq 0$  ( $U_{sl,L} \neq U_{sl,R}$ ), thereby inducing a competition between buoyancy driven and advection governed flow structures.

A high liquid co-flow (left) resulted in an initially fast rising bubble swarm (also left), which then, dependent on the initial gas fractions of both streams, might accelerate (Figs. 10a, 10d and 12a or decelerate (Figs. 10b, 10c, 10e, 10f and Figs. 12b, 12c, 12e, 12f) after the trailing edge of the splitter plate. In the latter cases, with a uniform aeration (Figs. 10b, 10e, and Figs. 12b, 12e. and with a higher  $U_{sg,R}$  (Figs. 10c, 10f, and Figs. 12c, 12f, a strong liquid co-flow originating from the left inlet (with a lower gas fraction) broadened and decelerated. This was due to entrainment of liquid into the bubbly flow rising from the right inlet, leaving just a narrow zone with a higher gas fraction at the far right. Under specific circumstances (see Fig. 12d and black markers in Fig. 15b) at  $\lambda_g = -1$ ) all bubbles rise more or less rectilinear because the gas fractions left and right are more or less equal.

By invoking Eq. (9), along with Eqs. (5) and (6) for  $\lambda_g$  and  $\lambda_l$ , respectively, the condition

$$\alpha_L = \alpha_R \tag{10}$$

can be converted into

$$\lambda_g = \lambda_l \frac{1}{1 + \xi \frac{U_l}{\langle U_{sl} \rangle}} \tag{11}$$

showing how for a specific value of  $\langle U_{sl} \rangle$  non-uniformities in aeration rate and liquid co-flow may neutralize each other and result in a quasi-uniform flow behavior.

As Part I of this twin paper showed that  $\alpha$  developed with respect to the height in the column (for uniform gas sparging), it cannot be assumed that Eqs. (10)-(11), with  $\xi = 0.82$ , work properly to estimate operating conditions for which the gas fractions for the left and right inlets at gas sparger level are equal. In our experiments, we only measured gas fractions at two positions at  $y = 63$  cm, see again Fig. 15. Rather than requiring the condition

of Eq. (10) to be imposed at the level of the sparger, we now apply this condition to the two measuring positions at  $y = 63$  cm. Therefore, operating conditions for which  $\alpha_{x=-15}(\triangleleft) = \alpha_{x=15}(\triangleright)$  are interpolated and indicated as circles in Figs. 15a and 15b. It is then assumed that if  $\alpha_{x=-15} = \alpha_{x=15}$ , there is also no gas fraction difference at the inlet ( $y = 0$ ), and buoyancy driven flow patterns will not develop.

Fitting of the interpolated values of  $\lambda_g$  to Eq. (11) yields  $\xi = 1.05 \pm 0.02$ , and Eq. (10) with  $\xi = 1.05$  may be used to describe the gas fraction at inlet conditions. As a higher value of  $\xi$  results in a lower estimated gas fraction, this agrees well with the findings of Part I of this paper, where lower gas fractions were found at a height of 40 cm above the sparger as compared to 80 cm (the sparger is located at  $y = -17$  cm). This can be explained due to a lesser degree of swarming behavior in the vicinity of the sparger as the array of bubble trains (of uniform, separately formed bubbles) was developing in the vicinity of the sparger and did not mix up to a height of at least 5 cm above the needle outlets (dependent on  $U_{sg}$  and  $U_{sl}$ ). More experiments are required to study a-symmetric operating conditions for which the (initial) gas fractions at both inlets are exactly equal.

#### 4.4.2. Bubble velocities

Locally measured bubble velocities in the presence of an asymmetric liquid co-flow are presented separately in A.2 and compared with vertical (swarm) velocity components obtained via BIV.

#### 4.4.3. Bubble chord lengths

Fig. 16 shows the mean chord lengths  $\bar{c}$  at  $x = \pm 15$  cm and  $y = 63$  cm as a function of  $\lambda_g$  and  $\lambda_l = 0, -1, -2$  for (a)  $\langle U_{sl} \rangle = 0.1$  m/s; and (b)  $\langle U_{sl} \rangle = 0.2$  m/s. The white markers in Figs. 16a and 16b show bubble chord lengths obtained with a uniform liquid co-flow ( $\lambda_l = 0$ ) as shown by the grey and black markers in Figs. 7b and 7c respectively.

$\lambda_l$ [-]		0	-1	-2
$x$	-15	◁	◁	◁
$x$	15	▷	▷	▷

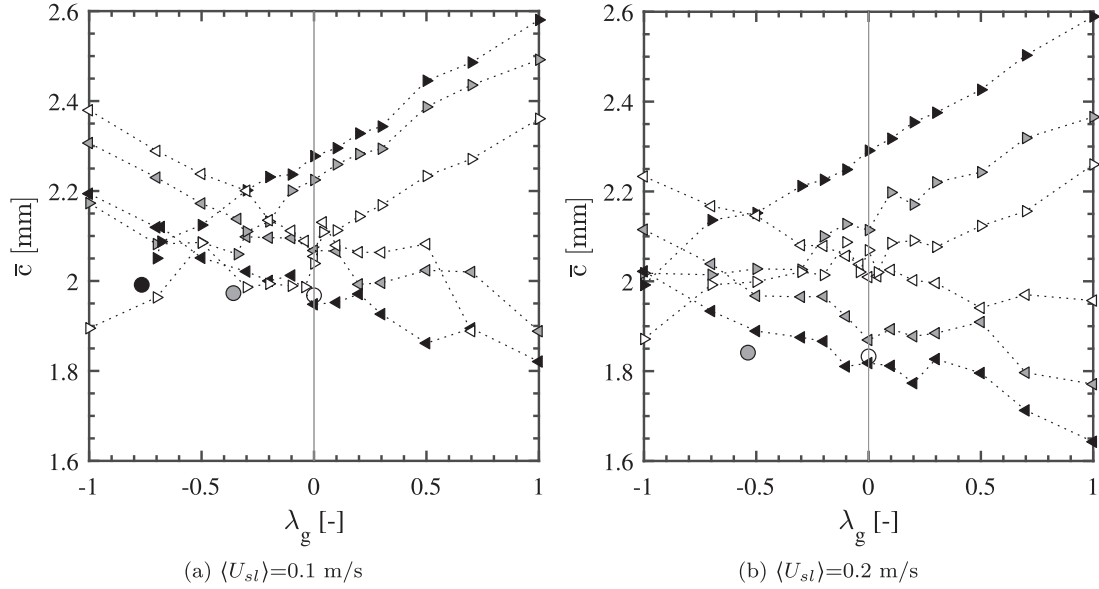


**Fig. 16.**  $\bar{\tau}$  as a function of the degree of asymmetry  $\lambda_g$  at  $x = \pm 15$  cm and  $y = 63$  cm for  $\lambda_l = 0, -1$  and  $-2$ .  $\langle U_{sg} \rangle = 1.25$  cm/s. The circular markers show the predicted chord lengths for operating conditions where  $d_{b,L} = d_{b,R}$ , see Eq. (12).

The largest bubbles were formed at the inlet with highest  $U_{sg}$  and lowest  $U_{sl}$ . Hence, the development of  $\bar{\tau}$  shows a similar trend as the development of  $\alpha$  shown in Fig. 15.

Operating conditions were predicted for which

$$d_{b,L} = d_{b,R} \quad (12)$$

where  $d_b = f(U_{sg}, U_{sl})$  was developed in our previous paper [Muilwijk and Van den Akker (2019b)]:

$$\frac{d_b}{d_n} = \left[ 0.093 \frac{U_l}{U_{g,n}} + \left( \left( \frac{6.18}{Bo} \right) + 1.26 Fr^{3/5} \right)^{-1} \right]^{-\frac{1}{3}} \quad (13)$$

where,

$$Bo = \frac{\rho_w g d_n^2}{\sigma} \approx 0.32 \quad (14)$$

$$Fr = \frac{U_{g,n}^2}{g d_n} \quad (15)$$

$U_{g,n}$  is the linear needle gas velocity,  $4Q_{g,n}/(\pi d_n^2)$ ,  $d_n$  the needle diameter ( $\varnothing = 1.55$  mm) and  $U_l$  the liquid co-flow velocity.

The values of  $d_b$  at the left and right inlet were calculated using the sectional (inlet) values for  $U_{sg}$  and  $U_{sl}$ , and  $U_{sg}$  is corrected for the hydrostatic pressure at gas sparger level (as a function of the overall gas hold-up). Operating conditions in terms of  $\lambda_g$ , for which Eq. (12) is satisfied, were calculated for  $\langle U_{sg} \rangle = 1.25$  cm/s,  $\langle U_{sl} \rangle = 0.1$  and  $0.2$  m/s and  $\lambda_l = -1, -2$ . These bubble diameters can be converted into chord lengths by taking a bubble shape factor of 0.50 (see Eqs. (5)-(6) of Part I). These chord lengths have been inserted into Figs. 16a and 16b as circular markers for the various  $\lambda_g$  values. The chord lengths calculated from Eqs. (12) and (13) agree rather well with the intersection points ( $\lambda_g$  values in Figs. 16a and 16b of the dotted lines through the experimental data.

Most calculated chord lengths, at the intersection points, were slightly smaller than the measured chord lengths. This can be explained by (1) the aspect ratio of 0.50 may be too small; (2) some uncertainty of  $d_b$  as predicted by Eq. (13); and (3) the bubble probes may be biased to larger chord lengths as bubbles pierced at the edge of a bubble are more likely to suffer from drifting.

#### 4.5. The apotheosis: An operating map

Fig. 17 summarizes the operating conditions of the experiments with an a-symmetric liquid co-flow as presented in this Section 4. The horizontal axis shows the superficial gas velocity and the vertical axis denotes the superficial liquid velocity. A triangle pointing left  $\triangleleft$  denotes the sectional inlet conditions of the left inlet, and a triangle pointing right  $\triangle>$  stands for the inlet conditions of the right inlet. The grey triangles show the experiments with  $\lambda_l = -1$ , whereas the black triangles denote the experiments with  $\lambda_l = -2$ . A thin gray/black line, hereafter operating line, connects the operating conditions of the left and right inlet for each experimental configuration. As all experiments were carried out at  $\langle U_{sg} \rangle = 1.25$  cm/s, the operating lines cross the operating points  $(\langle U_{sg} \rangle; \langle U_{sl} \rangle)$ . The two sets of radial spokes at  $(1.25; 0.1)$  and  $(1.25; 0.2)$  show the broad range of operating conditions and configurations we presented in this paper. Note that the operating points for the right inlet ( $\triangle>$ ) for  $\langle U_{sl} \rangle = 0.1$  and  $\langle U_{sl} \rangle = 0.2$  m/s coincide at  $U_{sl} = 0$  as  $U_{sl,R} = 0$  when  $\lambda_l = -2$ . The operating conditions for  $\lambda_l = 0$  (see Sec. 3) are omitted for clarity, as the operating lines would form horizontal lines in the range  $U_{sg} = 0.63 \dots 1.88$  cm/s through the operating points  $(\langle U_{sg} \rangle; \langle U_{sl} \rangle) = \{(1.25, 0); (1.25, 0.1); \text{ and } (1.25, 0.2)\}$ .

The gas fractions at the inlet, as a function of the sectional (left or right)  $U_{sg}$  and  $U_{sl}$  are calculated according Eq. (9) with  $\xi = 1.05$ . The iso-contours of the gas fraction at the inlet is shown by black solid (each interval of 1%) and dashed lines (each interval of 0.25%) and annotated outside the contour in Fig. 17. When an operating line is in parallel with the (solid/dashed black) contour lines for

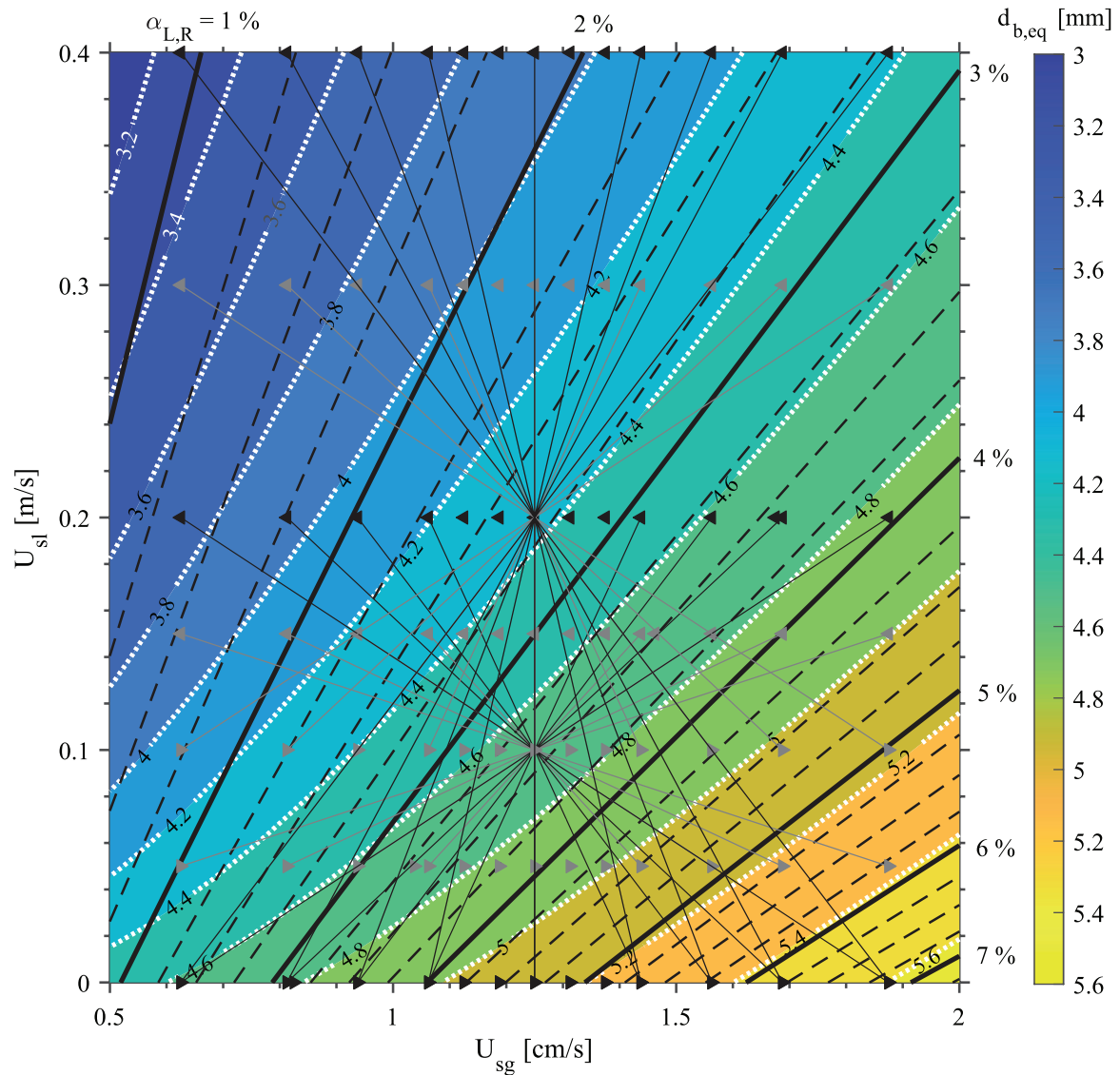


**Fig. 17.** Operating map as a function of the sectional  $U_{sg}$  and  $U_{sl}$ . Contour plot of  $d_b$  according to the correlation proposed in Muilwijk and Van den Akker (2019b). Dashed white contours are drawn at an interval of 0.2 mm. The black contours show conditions for which  $\alpha_l = \alpha_r$  and the numbers denote the gas fraction at the inlet calculated according to Eq. (9) with  $\xi = 1.06$ . Dashed black lines are drawn at each 0.25% interval. Grey markers:  $\lambda_l = -1$ ; black markers:  $\lambda_l = -2$ . The thin solid grey/black lines connect the operating conditions of the left inlet ( $\triangleleft$ ) to the operating conditions of the right inlet ( $\triangleright$ ) for each setting  $\lambda_g, \lambda_l$ , and  $(U_{sl})$ .

the void fraction, the void fraction of the left and right inlet is balanced and Eq. (10) is satisfied. For these cases, no buoyancy driven flow structures emerged and "bubbly mixing layer" conditions can be predicted. On the contrary, when the operating lines are rather skew, or even more or less normal, to the isocontours of  $\alpha_{L,R}$ , large contrasts of  $\alpha$  were imposed at the trailing edge of the splitter plate and the flow patterns were governed by buoyancy differences.

The colored contour map, with the white dotted isocontours, shows the bubble size as a function of the sectional  $U_{sg}$  and  $U_{sl}$ , see Eq. (13). Similarly, when the operating line is parallel to the isocontours of  $d_b$ , bubbles from the left and right inlet are formed with an equal equivalent diameter (but at a different formation rate). The conditions for which  $c_{x=-15} = c_{x=15}$  (then assuming  $d_{b,x=-15} = d_{b,x=15}$ ) do not necessarily coincide with the conditions for which  $\alpha_{x=-15} = \alpha_{x=15}$ . Therefore, regimes in Fig. 17 can be identified for which the isocontours of  $d_{b,L,R}$  and  $\alpha_{L,R}$  are (almost) parallel and operating conditions can be predicted for which a bubbly mixing layer pattern occurs (without buoyancy difference driven flow

structures). The lines connecting the points (1.88;0.4) and (0.63;0) for the case  $\langle U_{sg} \rangle = 1.25$  m/s;  $\langle U_{sl} \rangle = 0.2$  m/s;  $\lambda_g = -1$ ;  $\lambda_l = -2$ , are very parallel to both the isocontours of  $d_b$  and  $\alpha_{L,R}$  and the flow patterns in these cases approximated a bubbly mixing configuration, see Fig. 12d.

Fig. 17 offers an excellent starting-point for (transient) CFD two-fluid simulations of bubbly flows with the view to validate the models for phase interaction forces, two-phase flow turbulence and lateral bubble dispersion (the latter particularly due to differences in bubble velocities). First of all, Fig. 17 presents data for gas fraction and bubble size as functions of superficial gas and liquid velocities under various a-symmetric aeration and (non-)uniform liquid co-flow conditions. An interesting option would be to simulate various cases on e.g. the line connecting the points (1.88;0.4) and (0.63;0), to see whether such simulations would result in flow fields resembling Fig. 12d, in spite of different superficial gas and liquid velocities. Similarly, simulating cases on a line skew to the isocontours of  $\alpha_{L,R}$  should show the dynamics of buoyancy driven flow structures. The varying operating parameters for the left and

right inlet, leading to either a smooth mixing layer pattern (as in Fig. 12d) or buoyancy driven flow structures, provide a real challenge for simulations in which the contributions of the three above types of models may vary.

## 5. Conclusions

An experimental investigation of a-symmetric bubble column configurations was performed, with uneven gas sparging and with a uniform or a-symmetric liquid co-flow. Under several conditions, Kelvin-Helmholtz instabilities were observed developing into organized vortical flow structures as a result of lateral differences in mixture velocities and/or void fraction (i.e., mixture density).

Bubble streaks were captured in order to study the occurrence of (buoyancy driven) vortex roll-up structures. Bubble Image Velocimetry (BIV), an image correlation technique to calculate the displacement of parcels of bubbles, was then used to capture global flow patterns. Dual-tip optical fibre probes (OFP) were used to measure local void fractions, bubble velocities and chord lengths at two fixed positions in the column where the bubbles move predominantly upwards and aligned with the probe.

The vertical bubble velocity and standard deviation thereof, as measured using BIV and the OFPs, were compared and generally good agreement was observed between both methods. Contour plots of the bubble parcel velocity magnitude and the root-mean-square (RMS) of its velocity fluctuations were shown for a wide range of a-symmetric operating conditions.

We presented a thorough analysis of the steep departure from homogeneous bubbly flow to inhomogeneous bubbly flow as a function of a-symmetric gas sparging. It was found that a uniform liquid co-flow stabilized a slightly inhomogeneously sparged bubble column as the developing flow patterns were less sensitive to a (small) degree of a-symmetric sparging.

A model for the gas fraction was adopted to describe the gas fraction at the inlet as a function of both the degree of a-symmetric sparging and the degree of a-symmetric liquid co-flow. Operating conditions were identified for which there are no initial gas fraction differences, such that no buoyancy driven flow structures emerged. In this case, the bubbles move essentially rectilinear due to advection and a mixing layer pattern (with its development aligned with the splitter plate) was visible from the contours of the bubble velocity magnitude and RMS fluctuations. For all other cases, when the gas fraction of the left and right inlet were not equal, the bubble swarm originating from the inlet with the highest gas fraction always accelerated as a result of buoyancy differences and triggered large and unstable flow instabilities.

An operating map was constructed to plot the gas fraction at the inlet and the bubble diameter as functions of the sectional  $U_{sg}$  and  $U_{sl}$  and to represent all the experiments carried out with an a-symmetric liquid co-flow. This operating map can be very useful to identify regimes at which both inlets operate at equal gas fraction (and equal bubble diameter), such that there is no competition between buoyancy driven and advection driven flow structures or opposite. For future reference, operating conditions may be predicted for which mixing layer patterns occur in order to disentangle the effect of shear generated turbulence and bubble induced turbulence.

Future work may include further analysis of (the obtained) BIV data to study the dynamics of the bubble column, by means of Proper Orthogonal Decomposition and/or Dynamic Mode Decomposition. Also, regimes can be identified for which the mean bubble velocities can be described by a parametric error function in terms of  $x$ ,  $y$ , and the operating conditions.

A further experimental analysis may focus on Laser Doppler Velocimetry or phase-sensitive Hot-Wire Anemometry (when optical access is impeded due to the high void fraction) to study liquid

velocities and turbulence. The bubble (parcel) velocities presented here may then act as a reference for calculating (local) slip velocities.

## Declaration of Competing Interest

The authors declare that they have no conflict of interest.

## CRediT authorship contribution statement

**Corné Muilwijk:** Conceptualization, Methodology, Software, Validation, Formal analysis, Investigation, Writing - original draft, Visualization. **Harry E.A. Van den Akker:** Conceptualization, Writing - review & editing, Supervision, Funding acquisition.

## Acknowledgements

This research was made possible through a start-up fund in the context of the Bernal Project at the University of Limerick. The authors want to acknowledge Saikat Bhowmick MSc. for his assistance during the experiments.

## Appendix A. Bubble velocities and parcel velocities

### A1. The effect of a uniform-coflow ( $\lambda_l = 0$ )

Fig. A.1 shows the mean bubble velocity  $\bar{v}_b$  as measured with the dual-tip optical fibre probes (a) and parcel velocities as obtained by using BIV (b) as a function of the degree of a-symmetric gas sparging  $\lambda_g$  for  $\langle U_{sl} \rangle = 0$  (open markers); 0.1 (grey markers) and 0.2 m/s (black markers). The optical fibre probe measurements at  $x = -15$  and  $x = +15$  cm were taken simultaneously (300 s average). The bubble parcel velocities (10 s average) at  $y = 63$  cm were linearly interpolated at  $x = \pm 15$  cm from the profiles as shown in Fig. 5. It should be noted that a triangle pointing right ( $\triangleright$ ) denotes the measurements at location at  $x = +15$  cm, whereas a triangle pointing left ( $\triangleleft$ ) denotes measurements at  $x = -15$  cm.

In general, good agreement was observed between the bubble (parcel) velocities as obtained by both methods. In line with Part I of this paper, both methods agree very well at intermediate bubble velocities ( $20 < \bar{v}_b < 40$  cm/s), whereas BIV results in velocities up to 15% higher for  $\bar{v}_b > 60$  cm/s. As the Optical Fibre Probes are centered between the front and rear wall, while the depth of view of the camera covered the whole depth of the column, this discrepancy can be ascribed due to 3D effects as the BIV results may be biased to the flow in the vicinity of the front column wall (especially for higher  $\alpha$  when the transparency decreased). Gradients of  $\alpha$  and  $v_b$  in the collinear direction (between front and rear wall) may compromise the comparability of both methods and further (numerical) research is required to study the validity of a 2D ( $x, y$ ) flow assumption.

Without liquid co-flow, the bubble velocity is hugely sensitive to a small degree of a-symmetric gas sparging (see white markers around  $\lambda_g = 0$  in Fig. A.1), even more strongly than alpha (in Fig. 6). Also from the development of  $\bar{v}_b$  as a function of  $\lambda_g$ , it can be seen that the line of symmetry is slightly to the right of  $\lambda_g = 0$  due to a slight imbalance of the Mass Flow Controller calibrations. A-symmetric sparging induces a global liquid recirculation loop. The stream originating from the inlet with the highest gas fraction accelerates and entrains fluid. This entrained fluid comes down at the other side of the column. The downward velocity of the liquid drags bubbles down the column, hence negative bubble velocities are realistically obtained from the BIV method. Due to the configuration of the optical fibre probes, small (and negative) bubble velocities could not be measured. Bubble velocity measurements using the optical probe for the set for  $U_{sl} = 0$  m/s (Fig. A.1a) were ig-

$\langle U_{sl} \rangle$ [m/s]	0	0.1	0.2
x	-15	◁	◀
y	15	▷	▶

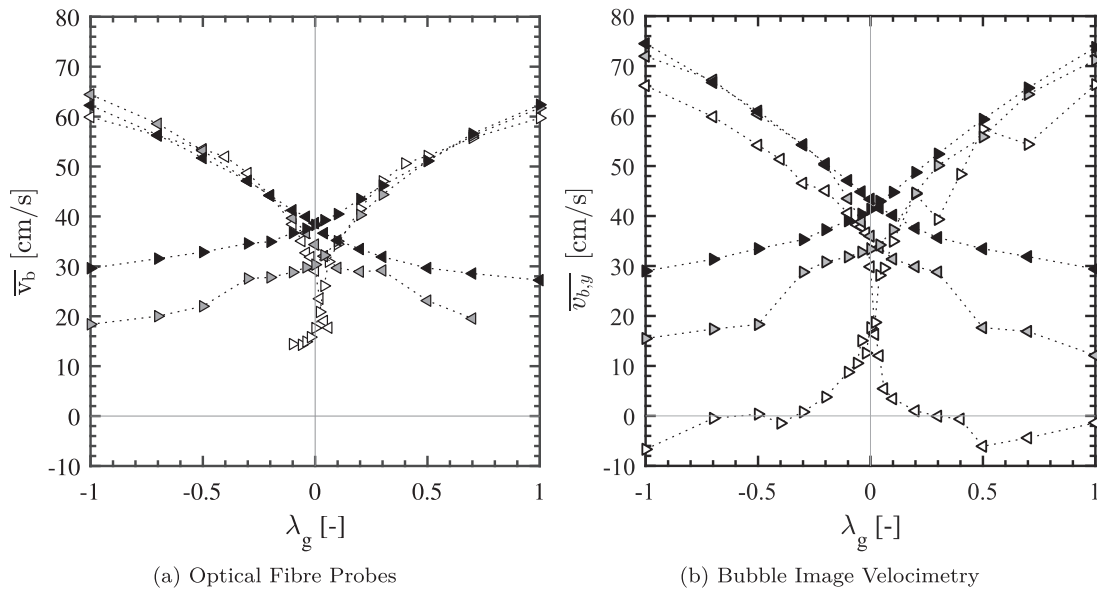


Fig. A.1.  $\bar{v}_b$  at  $x = \pm 15$  cm and  $y = 63$  cm as a function of the degree of asymmetry  $\lambda_g$ . Left: Optical fibre probe; Right: Bubble Image Velocimetry.  $\langle U_{sg} \rangle = 1.25$  cm/s;

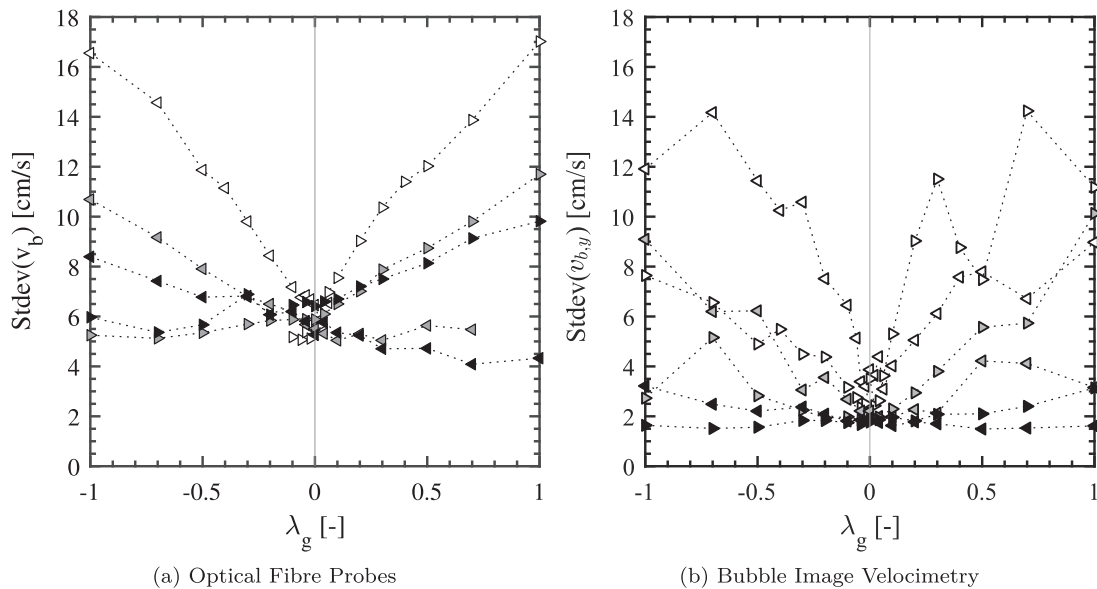


Fig. A.2.  $Stdev(v_b)$  at  $x = \pm 15$  cm and  $y = 63$  cm as a function of the degree of asymmetry  $\lambda_g$ .  $\langle U_{sg} \rangle = 1.25$  cm/s;

nored when insufficient valid bubble velocity measurements were obtained.

With increasing  $\langle U_{sl} \rangle$ , the measured velocities at the two monitoring points in Fig. A.1 deviated to a lesser degree from the more homogeneous flow conditions at  $\lambda_g = 0$ , as already shown in Fig. 3, while they are less sensitive to small variations in  $\lambda_g$ . This is due the reduction of the occurrence of (fluctuating) recirculation loops.

Fig. A.2 shows the standard deviation of the bubble velocity  $Stdev(v_b)$  as measured with the dual-tip optical fibre probes (a) and parcel velocities as obtained by using BIV (b) as a function of

the degree of a-symmetric gas sparging  $\lambda_g$  for the same cases as outlined in Fig. A.1. Similar to the development of  $\alpha$  (Fig. 6) and  $\bar{v}_b$  (Fig. A.1) as a function of  $\lambda_g$ , also the evolution of  $Stdev(v_b)$  is very symmetric with respect to  $\lambda_g = 0$ . The standard deviations obtained from the BIV method (b) show a more irregular behavior than those obtained by the optical fibre probes (a) as the sampling period of the BIV is 10 s, compared to the 300 s duration of the bubble probe data acquisition. The observed trends in  $Stdev(v_b)$  as captured by both OFP and BIV methods are rather similar. Although the standard deviations of the velocity distributions measured by

$\lambda_1$ [-]	0	-1	-2
$x$	$\triangleleft$	$\triangleleft$	$\blacktriangleleft$
$y$	$\triangleright$	$\triangleright$	$\blacktriangleright$

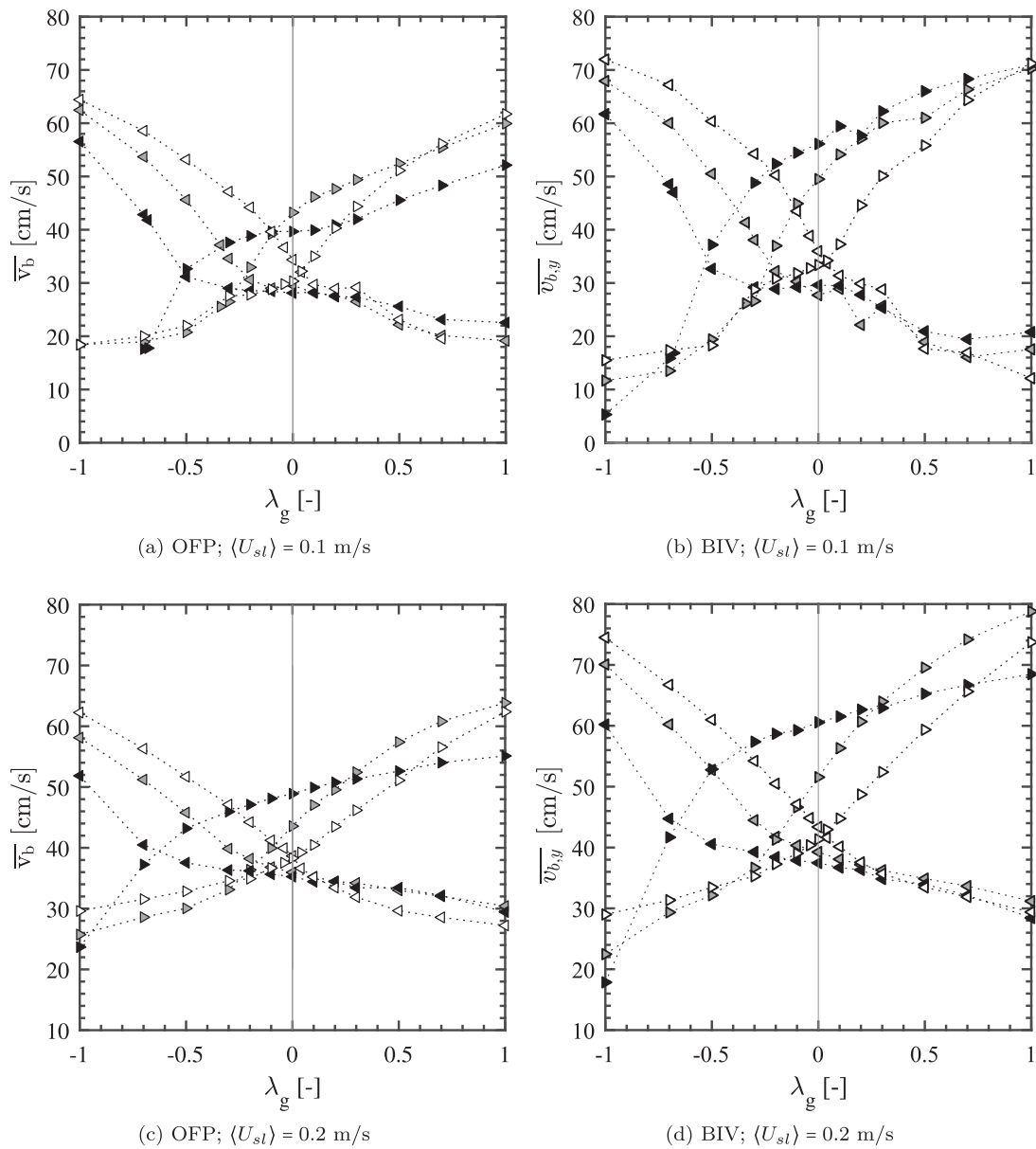


**Fig. A.3.**  $\bar{v}_b$  as a function of the degree of asymmetry  $\lambda_g$  at  $x = \pm 15$  cm and  $y = 63$  cm for  $\lambda_1 = 0, -1$  and  $-2$ . Top:  $\langle U_{sl} \rangle = 0.1$ ; and bottom:  $0.2$  m/s. Left: Optical fibre probe; Right: Bubble Image Velocimetry.  $\langle U_{sg} \rangle = 1.25$  cm/s.

the optical fibre probes are  $\approx 3$  cm/s higher than those obtained using BIV. This difference is ascribed to the wobbling behavior of the bubble interfaces (see also Part I).

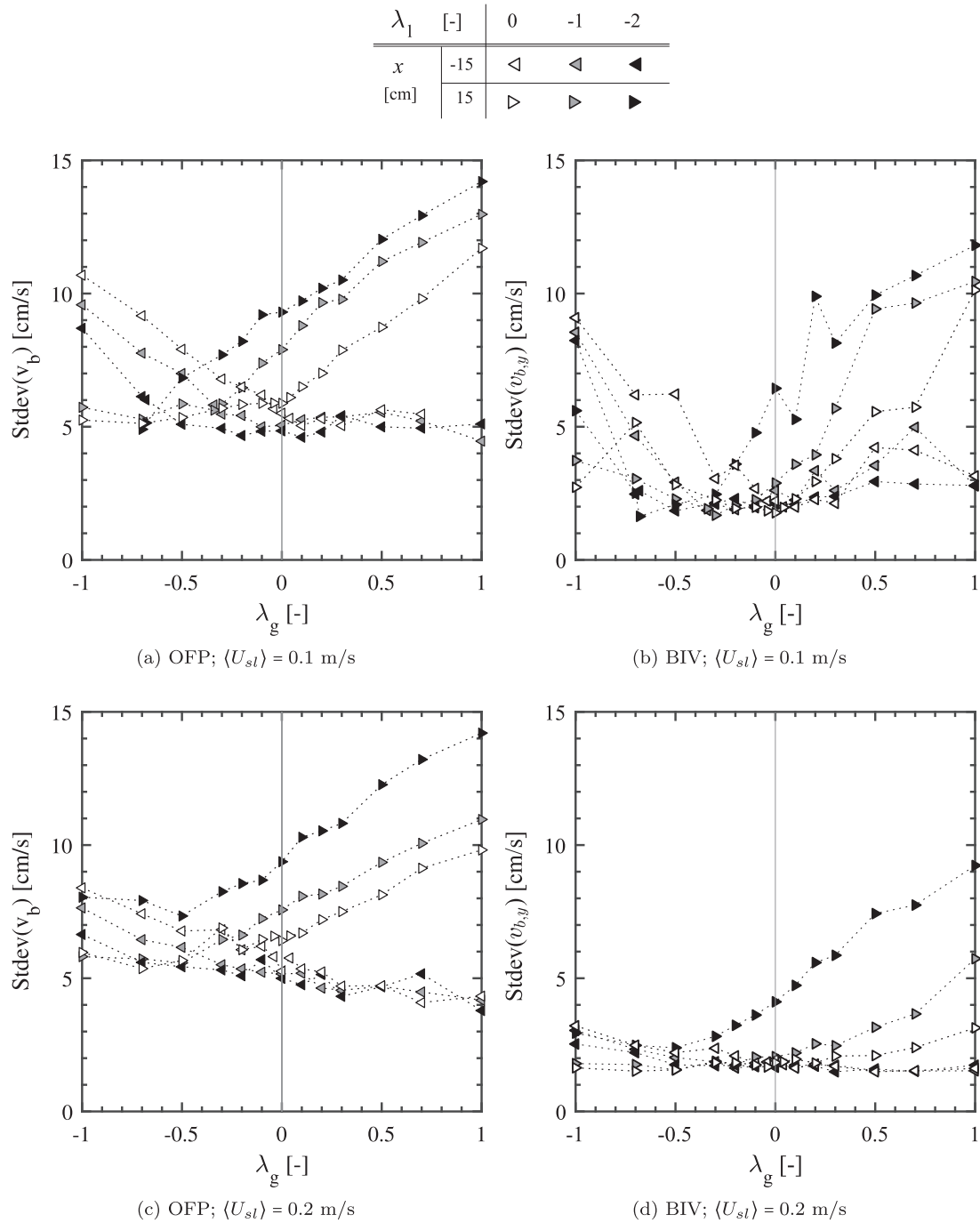
**A2. The effect of a non-uniform-coflow ( $\lambda_1 < 0$ )**

Fig. A.3 shows bubble velocities as measured by the OFPs (left) and BIV (right) at  $x = \pm 15$  cm and  $y = 63$  cm as a function of  $\lambda_g$  for  $\lambda_1 = 0, -1$  and  $-2$ . The top row shows results for  $\langle U_{sl} \rangle = 0.1$  m/s, whereas  $\langle U_{sl} \rangle = 0.2$  m/s for the bottom row.

The development of  $\bar{v}_b$  as a function of  $\lambda_g$  and  $\lambda_1$  show a similar trend as  $\alpha$  shown in Fig. 15. A high gas fraction induces a buoyancy

driven acceleration of the bubble plume, hence mostly a higher  $\bar{v}_b$  was measured if the region where the gas fraction was high.

Similar curves were obtained from the OPF and BIV method. BIV results in relatively higher velocities for the regions with a  $\bar{v}_b$  and  $\alpha$ , which is consistent with the results obtained in Part I and with Fig. A.1 of this paper. As the gradients of  $\bar{v}_b$  are high in the (fluctuating) boundary region, BIV may not give a sufficiently accurate statistical average, while also a uni-directional flow assumption for the OFP measurements may be invalid. As, due to the current camera configuration, the whole depth of the column was in focus, a mapping error may occur when converting position to a coordinate. As the transparency is a function of the bubble number den-



**Fig. A.4.**  $\text{Stdev}(v_b)$ , as a function of the degree of asymmetry  $\lambda_g$  at  $x = \pm 15$  cm and  $y = 63$  cm for  $\lambda_l = 0, -1$  and  $-2$ . Top:  $\langle U_{sl} \rangle = 0.1$  m/s; bottom:  $\langle U_{sl} \rangle = 0.2$  m/s. Left: Optical fibre probe; Right: Bubble Image Velocimetry.  $\langle U_{sg} \rangle = 1.25$  cm/s.

sity, measurements are biased to the flow in the vicinity of the front wall for high gas fractions, while bubbles at the back wall of the column (having a different mm/pix) became visible for lower gas fractions. This may have a considerable effect in regions of high velocity gradients at the edges of the domain.

Fig. A.4 shows bubble velocity fluctuations as measured by the OFPs (left) and parcel velocity fluctuations measured using BIV (right) at  $x = \pm 15$  cm and  $y = 63$  cm as a function of  $\lambda_g$  for  $\lambda_l = 0, -1$  and  $-2$ . The top row shows results for  $\langle U_{sl} \rangle = 0.1$  m/s, whereas  $\langle U_{sl} \rangle = 0.2$  m/s for the bottom row.

Although higher bubble velocity fluctuations are measured by the OFPs, both methods (OFP and BIV) show similar trends. As OFP

measurements were taken for 300 s, the development of  $\text{Stdev}(v_b)$  is very smooth. The length of BIV measurements was 10 s and somewhat less smooth trends were found for the results shown in Fig. A.4b. However, a smooth development of  $\text{Stdev}(v_b)$  was recovered when  $\langle U_{sl} \rangle$  was increased to 0.2 m/s (see Fig. A.4d), as a stronger co-flow more clearly determined flow structures.

For all cases, strong velocity fluctuations were measured at  $x = 15$  cm ( $\triangleright$ ) for  $\lambda_g > 0$ . As the boundary (strongly) developed to the right side for  $\lambda_g > 0$  (and  $\lambda_l < 0$ ), the OFP at  $x = 15$  cm measured in the close vicinity of the boundary and it can be seen that  $\text{Stdev}(v_b)$  increased gradually with an increasing degree of asymmetric liquid co-flow,  $\lambda_l$ . As concluded from the gradual trends

in Fig. A.4, no sharp operating regime transition exists between a flow pattern with a steady or unsteady boundary.

For  $\lambda_g < 0$ ,  $Stdev(v_b)$  converges to a situation with similar root mean square velocity fluctuations as under homogeneous gas sparging and liquid co-flow. These operating conditions seem to occur in the proximity for conditions for which Eq. (10) is valid, e.g. the left and right inlet gas fractions are almost equal and the boundary remains centered and a mixing layer configuration is restored.

### Supplementary material

Supplementary material associated with this article can be found, in the online version, at doi:[10.1016/j.ijmultiphaseflow.2021.103562](https://doi.org/10.1016/j.ijmultiphaseflow.2021.103562).

### References

- Alm eras, E., Plais, C., Roig, V., Risso, F., Augier, F., 2018. Mixing mechanisms in a low-sheared inhomogeneous bubble column. *Chemical Engineering Science* 186, 52–61. doi:[10.1016/j.ces.2018.04.026](https://doi.org/10.1016/j.ces.2018.04.026).
- Ayed, H., Chahed, J., Roig, V., 2007. Hydrodynamics and mass transfer in a turbulent buoyant bubbly shear layer. *AIChE J.* 53 (1), 2742–2753. doi:[10.1002/aic](https://doi.org/10.1002/aic).
- Becker, S., Sokolichin, A., Eigenberger, G., 1994. Gasliquid flow in bubble columns and loop reactors: Part ii. comparison of detailed experiments and flow simulations. *Chemical Engineering Science* 49 (24, Part 2), 5747–5762. doi:[10.1016/0009-2509\(94\)00290-8](https://doi.org/10.1016/0009-2509(94)00290-8).
- Brown, G.L., Roshko, A., 1974. On density effects and large structure in turbulent mixing layers. *Journal of Fluid Mechanics* 64 (04), 775–816. doi:[10.1017/S002211207400190X](https://doi.org/10.1017/S002211207400190X).
- De Tournemine, A.L., Roig, V., 2010. Self-excited oscillations in buoyant confined bubbly mixing layers. *Physics of Fluids* 22 (2), 023301. doi:[10.1063/1.3327290](https://doi.org/10.1063/1.3327290).
- Groen, J., Oldeman, R., Mudde, R., Van den Akker, H.E.A., 1996. Coherent structures and axial dispersion in bubble column reactors. *Chemical Engineering Science* 51 (10), 2511–2520. doi:[10.1016/0009-2509\(96\)00110-8](https://doi.org/10.1016/0009-2509(96)00110-8).
- Gvozdi c, B., Dung, O.-Y., Alm eras, E., van Gils, D.P., Lohse, D., Huisman, S.G., Sun, C., 2019. Experimental investigation of heat transport in inhomogeneous bubbly flow. *Chemical Engineering Science* 198, 260–267. doi:[10.1016/j.ces.2018.09.040](https://doi.org/10.1016/j.ces.2018.09.040).
- Gvozdi c, B., Dung, O.-Y., van Gils, D.P.M., Bruggert, G.-W.H., Alm eras, E., Sun, C., Lohse, D., Huisman, S.G., 2019. Twente mass and heat transfer water tunnel: Temperature controlled turbulent multiphase channel flow with heat and mass transfer. *Review of Scientific Instruments* 90 (7), 075117. doi:[10.1063/1.5092967](https://doi.org/10.1063/1.5092967).
- Harteveld, W.K., 2005. *Bubble columns: Structures or stability?*. Delft University of Technology, Delft, The Netherlands.
- Harteveld, W.K., Mudde, R.F., Van Den Akker, H.E.A., 2003. Dynamics of a Bubble Column: Influence of Gas Distribution on Coherent Structures. *The Canadian Journal of Chemical Engineering* 81 (3-4), 389–394. doi:[10.1002/cjce.5450810308](https://doi.org/10.1002/cjce.5450810308).
- Huang, Z., McClure, D.D., Barton, G.W., Fletcher, D.F., Kavanagh, J.M., 2018. Assessment of the impact of bubble size modelling in CFD simulations of alternative bubble column configurations operating in the heterogeneous regime. *Chemical Engineering Science* 186, 88–101. doi:[10.1016/j.ces.2018.04.025](https://doi.org/10.1016/j.ces.2018.04.025).
- Loth, E., Cebrzynski, M., 1995. Modulation of shear layer thickness due to large bubbles. *International journal of multiphase flow* 21 (5), 919–927.
- McClure, D.D., Dolton, T.P., Barton, G.W., Fletcher, D.F., Kavanagh, J.M., 2017. Hydrodynamics and mixing in airlift contactors: Experimental work and CFD modelling. *Chemical Engineering Research and Design* 127, 154–169. doi:[10.1016/j.cherd.2017.09.020](https://doi.org/10.1016/j.cherd.2017.09.020).
- McClure, D.D., Wang, C., Kavanagh, J.M., Fletcher, D.F., Barton, G.W., 2016. Experimental investigation into the impact of sparger design on bubble columns at high superficial velocities. *Chemical Engineering Research and Design* 106, 205–213. doi:[10.1016/j.cherd.2015.12.027](https://doi.org/10.1016/j.cherd.2015.12.027).
- Mudde, R., Van Den Akker, H., 1999. Dynamic behavior of the flow field of a bubble column at low to moderate gas fractions. *Chemical Engineering Science* 54 (21), 4921–4927. doi:[10.1016/S0009-2509\(99\)00213-4](https://doi.org/10.1016/S0009-2509(99)00213-4).
- Muilwijk, C., Van den Akker, H.E.A., 2019. Experimental investigation on the bubble formation from needles with and without liquid co-flow. *Chemical Engineering Science* 202, 318–335. doi:[10.1016/j.ces.2019.03.026](https://doi.org/10.1016/j.ces.2019.03.026).
- Muilwijk, C., Van den Akker, H.E.A., 2019. The Limerick bubbly flow rig: Design, performance, hold-up and mixing pattern. *Chemical Engineering Research and Design* 152, 106–122. doi:[10.1016/j.cherd.2019.09.021](https://doi.org/10.1016/j.cherd.2019.09.021).
- Muilwijk, C., Van den Akker, H.E.A., 2020. The effect of liquid co-flow on gas fractions, bubble velocities and chord lengths in bubbly flows. part i: Uniform gas sparging and liquid co-flow. *International Journal of Multiphase Flow* 103498. doi:[10.1016/j.ijmultiphaseflow.2020.103498](https://doi.org/10.1016/j.ijmultiphaseflow.2020.103498).
- Ning, T., Guo, F., Chen, B., Zhang, X., 2009. PIV measurement of turbulent bubbly mixing layer flow with polymer additives. *Journal of Physics: Conference Series* 147, 012014. doi:[10.1088/1742-6596/147/1/012014](https://doi.org/10.1088/1742-6596/147/1/012014).
- Rietema, K., 1982. *Science and technology of dispersed two-phase systems i and ii*. *Chemical Engineering Science* 37 (8), 1125–1150.
- Roig, V., Suzanne, C., Masbernat, L., 1998. Experimental investigation of a turbulent bubbly mixing layer. *International Journal of Multiphase Flow* 24 (1), 35–54. doi:[10.1016/S0301-9322\(97\)00046-3](https://doi.org/10.1016/S0301-9322(97)00046-3).
- Van Den Akker, H.E.A., 1998. Coherent structures in multiphase flows. *Powder Technology* 100 (2-3), 123–136. doi:[10.1016/S0032-5910\(98\)00133-8](https://doi.org/10.1016/S0032-5910(98)00133-8).
- Winant, C.D., Browand, F.K., 1974. Vortex pairing : the mechanism of turbulent mixing-layer growth at moderate Reynolds number. *Journal of Fluid Mechanics* 63, 237–255. doi:[10.1017/S0022112074001121](https://doi.org/10.1017/S0022112074001121).